Internal Wave Interaction with Broad Topography in the Presence of a Near-Bottom Stratification

by

Sandhya Harnanan

A thesis
presented to the University of Waterloo
in fulfillment of the
thesis requirement for the degree of
Master of Mathematics
in
Applied Mathematics

Waterloo, Ontario, Canada, 2016

I hereby declare that I am the sole author of this thesis. This is a true copy of the thesis, including any required final revisions, as accepted by my examiners.

I understand that my thesis may be made electronically available to the public.

Abstract

This thesis considers the impact of internal waves on the transport of suspended matter across the bottom boundary layer. High resolution two- and three-dimensional direct numerical simulations of fully nonlinear, laboratory-scale internal solitary waves propagating over broad topography with a near-bottom stratified layer are presented. A near-bottom stratification is used to represent a nepheloid layer, or a layer of previously suspended material found near the bottom. The three-dimensional, mapped coordinate, spectral allocation method employed in the simulations allows for accurate modelling of the near-boundary dynamics. Noise of two amplitudes are used to initialize the three-dimensional simulations, as the natural world has a broad range of naturally occurring "noise". Both waves of depression and elevation are considered and the formation of the two distinct types of instabilities that result is discussed. The prograde jet at the back of the wave of depression rolls up at the hill crest, with subsequent vortex production. When a near-bottom stratification is present, the resulting vortex structures are smaller, less energetic and more confined to the hill when compared to an unstratified bottom. However, the instabilities still provide a means for transport across the bottom boundary layer in a significant geographical area. In the case of a wave of elevation, a novel type of gravity current forms in the near-bottom region as the wave moves over the topography. There is intense mixing of fluid in the leading edge of the current that moves along with the wave and also provides a means for transport across the bottom boundary layer. The effects of the two noise amplitudes are considered for each type of wave. Finally, a very brief extension of the results to the field-scale is presented.

Acknowledgements

There are so many people who made this journey and venture of my life a reality. I will try my best to include everyone; if I forget anyone, please pardon me and know that I am thankful. First up, I would like to express my heartfelt thanks and gratitude to my supervisor, Professor Marek Stastna, for this amazing opportunity. Thank you for teaching and guiding me, and most of all, thank you for recognizing my potential and believing in me. I don't know what I did to catch your eye during my third year of undergrad while taking your Continuum Mechanics course. Also, thank you so much for being understanding and accommodating towards the personal struggles that have emerged within the last two years. I sincerely appreciate it. At this point I can't yet clearly see what the future holds for my career, but no matter what happens, please know that your role in my life (no matter how small you may think it to be), is what helps to make my future possible.

Many thanks go out to my work colleagues for every little piece of help and advice that went into making this thesis what it is, and for an enjoyable Master's program. Special thanks goes to my office mates David, Ben and Will for their help with computational and Matlab matters, and for enlightening discussions. It was fun sharing an office with you guys. Xiaolin, your kindness is most appreciated. Thank you Lindsey for your honest critique on my figures, help with Latex; and for pita Fridays, of course. Thanks to all of the members of the Fluids Group, who have made my experience an enriching and worthwhile one. Thank you Mike Waite and Siv Sivaloganathan, my committee members for reading and reviewing my thesis, with your valuable comments and suggestions. Thank you Laura and Cyntia for ensuring that the administrative side of my Master's went smoothly. I would also like to thank Nancy for her help and inspiration while I worked as an undergrad research assistant with Marek. Also, thank you Aimy. You are a confidante and friend to whom I could have turned when I needed a break from my studies.

Finally and most importantly, I would like to thank my family. Thank you aunt Viola and uncle Arjoon for always keeping the door to your home open to me. You have been like parents to me during my stay in Canada. My most sincere and deepest thanks goes to my parents. It is without a doubt that what I have achieved thus far has been strongly influenced by the foundation which you have provided me with. Life is not always easy, as you have taught me, but you also taught me to be strong, and you gave me the support and encouragement whenever I needed it. Thank you for allowing me to follow my dreams.

Dedication

To my parents, to whom I am ever grateful for the continuous love, support and guidance given to me. I am truly blessed to have you in my life.

Table of Contents

List of Tables

List of Figures

Chapter 1

General Introduction

Naturally occurring fluids in the environment, be it the atmosphere, oceans or lakes, all possess stratification. A stratified fluid is one in which there is a density variation with the fluid depth. For the stratification to be statically stable, less dense fluid must overly more dense fluid. There is often a region with a sharp density gradient, referred to as a pycnocline. Density changes can arise from differences in salinity, temperature, or suspended sediment concentration. In the case that the density variations are due to temperature or salinity differences, the regions of sharp density gradients are called thermoclines or haloclines respectively. Stratified fluids are vital for the dynamical processes that occur in natural fluid bodies, and they open up a world of possibilities for instability phenomena. On larger scales, stratified fluids give rise to internal waves which then interact with a changing environment (e.g. shoaling over topography), resulting in a transfer of energy to smaller scale phenomena where there is three-dimensionalization, dissipation, and mixing.

1.1 Internal Solitary Waves

Internal waves are waves that occur in the interior of a stratified fluid; they exist because the restoring force of gravity acts on vertically displaced fluids. An internal solitary-like wave is a single internal wave that propagates at a constant speed without changing shape as it travels long distances. Only mode-1 internal solitary-like waves will be considered in this work, and the acronym "ISW" will be used to refer to such waves. Horizontally propagating ISWs can be classified as either waves of depression (a wave in which lines of constant density are lowered, i.e. a trough) or waves of elevation (a wave in which lines of constant density are raised, i.e. a crest). The type of ISW observed at a particular

location is determined by the location of the pycnocline and possibly background shear [37, 36, 61], although the latter will not be considered in this thesis. In the absence of shear, a pycnocline that is centred above the water column mid-depth results in waves of depression, whereas a pycnocline centred below the mid-depth is associated with waves of elevation [30, 41]. Since the density differences across the pycnocline within the same fluid are usually much smaller than the density difference across the interface between two fluids (e.g. air and water), the restoring forces are weaker for internal waves than surface waves. As such, for a given amount of energy, internal waves can achieve much larger amplitudes than surface waves.

ISWs can be detected in oceans as alternating light and dark bands through satellite imagery, which has shown that internal waves are a ubiquitous feature of coastal oceans. Observations of internal waves in the oceans have revealed that these waves are highly nonlinear [29] (see section 2.2 for more details). In the South China sea, waves with an amplitude to depth ratio as large as 0.44 have been observed (an approximate 150 m amplitude in a 340 m total depth, with an upper layer thickness of about 40 m) [18]. Other large-amplitude waves (22 m in 71 m depth) have also been detected off the Oregon coast [66]. In Lake Überlingen, a sub-basin of Lake Constance, Preusse *et al.* [51] measured a large-amplitude ISW train, where the amplitude of a wave of depression was as large as 30 m in a total depth of about 100 m.

It is important to study ISWs because of their impact on coastal marine environments and lake ecosystems. Internal waves can influence mixing, resuspend and transport sediment, including nutrients and chemicals, all of which can have an effect on optical and acoustical properties of the water column, water quality, and biological productivity in the local ecosystems. One of the main ways by which ISWs can do this is through their interaction with the bottom topography, on which there have been several studies.

Maderich *et al.* (2010) [42] and Talipova *et al.* (2013) [65] in two companion papers considered both ISWs of elevation and depression propagating over a bottom step topography. Maderich *et al.* concentrated on the interaction of ISWs of depression with a step that was large enough to induce a significant change in the incoming wave. For such cases, they found that wave-step interaction led to strong eddy generation that mixed fluid from below the step into the layer overlying the step. Talipova *et al.* focused on energy loss to dissipation, finding energy losses of up to 50% in extreme cases, with lower values being more typical. However, the results of these two studies may not accurately reflect what actually transpires in the field, because natural topography is much more gentle than step-like topography. More recently, Harnanan *et al.* (2015) [24] considered ISWs of depression and elevation propagating over gentle topography, finding that a wave of depression can be likely to provide an efficient means of pumping material out of the bottom boundary

layer (BBL) in a large geographical area. More details of Harnanan *et al.* [24] are given in section 3.2.

The role of ISWs in sediment resuspension has been addressed in studies such as Diamessis and Redekopp (2006) [17], Stastna and Lamb (2008) [62], Quaresma *et al.* (2007) [53], and Aghsaee and Boegman (2015) [2]. Diamessis and Redekopp [17] performed numerical simulations of both ISWs of elevation and depression propagating over a flat boundary. Their results indicated that for waves of a high enough amplitude, a global instability occurs in regions near the bottom boundary where the wave induces an adverse pressure gradient. The bursting of the separation bubble (see section 2.4) led to vortex formation, with the shed vortices from the bottom boundary reaching as high as 30% - 35% of the water depth, thus providing a means for sediment resuspension in shallow waters. However, there is a possible element of questionability regarding their results, because of the authors' use of weakly nonlinear theory for initializing their simulations. Nevertheless, the results for the instability behaviour in the bottom boundary layer (BBL) of Stastna and Lamb [62] were in qualitative agreement with Diamessis and Redekopp. Stastna and Lamb used fully nonlinear theory to simulate an ISW of elevation interacting with a barotropic background current as it propagated over a flat bottom, and found that periodic vortex ejection events moved particles more than 15% of the total water depth above the bottom. Their results also suggested that there is a potential for efficient sediment resuspension as the ISW of elevation (interacting with a barotropic current) propagates over an isolated hill. Neither of these studies consider the three-dimensional effects of the instabilities.

The recent laboratory experiments by Aghsaee and Boegman (2015) [2] looked at sediment resuspension induced by ISWs of depression propagating over a flat bed. They found that not only does the viscous bed shear stress need to exceed the critical value (the Shield's criterion) in order to resuspend sediment, but the vertical velocities need to be an order of magnitude larger than the settling velocity of the sediments. These necessary burst-like vertical velocity events which lift sediment into the water column occur in the adverse pressure gradient region beneath the trailing part of the wave. If the bed shear stress exceeded the critical value, but the vertical velocity was below the required limit, sediment and bed-load transport was observed, but resuspension was not. Aghsaee and Boegman also introduced a resuspension criterion based on bulk water column stratification, and wave and sediment characteristics, which they have found to be consistent with laboratory and field data.

Observations by Quaresma *et al.* (2007) [53] found that large-amplitude ISWs of depression were capable of eroding and resuspending sediment on the Portuguese shelf, thereby sustaining a $10 - 15$ m thick bottom nepheloid layer (BNL). Their measurements revealed that resuspension occurred when the maximum bed shear stress was five times greater than

the critical bed shear stress for a particular particle size. Interestingly, they also found that the ISWs could induce considerable vertical velocities ($0.025 - 0.1$ ms^{-1}) which interact with and thicken the BNL, even if the bottom shear stress was not high enough to erode sediment from the seabed. This is because the vertical velocities were able to pump the near-bottom suspended sediments to heights above the BNL.

Olsthoorn and Stastna (2014) [47], through simulations of waves propagating over an isolated hill, concluded that near-bed instabilities can affect chemical transport across the BBL, even in cases of no sediment resuspension. At the same time, Scalo *et al.* [55] suggested that 'scarring' of the boundary layer by coherent structures can enhance transport of passive tracers, such as suspended oxygen, across the boundary layer. Cross-BBL transport, where material is transported vertically across the edge of the boundary layer, and spread out either in the BBL or the overlying water column, is thus a process that is potentially as important to model correctly as sediment resuspension.

1.2 Nepheloid Layers

A nepheloid layer is a layer of increased suspended particulate matter, and is identified by its light scattering and light absorption properties [43]. Nepheloid layers are a common feature in the oceans and large lakes [28], and can be classified into different types depending upon where in the water column they occur. Benthic or bottom nepheloid layers (BNLs) form at the bottom of the water column, immediately above the sediment-water interface. Intermediate nepheloid layers (INLs) occur at mid-depths, and are usually associated with thermoclines or pycnoclines, whereas surface nepheloid layers (SNLs) occur at the surface of the water column [28].

The present work will consider BNLs, as instabilities near the bottom boundary are of primary interest to the author. BNLs are found in large lakes [27, 28, 40], at the base of continental slopes and on continental margins [43, 49, 69]. The structure, thickness, composition, and time variation of a BNL are influenced by several factors such as the local and regional fluid flow, bottom sediment type, particulate export from overlying waters, and local biological community composition [49, 28]. As a result, the formation and maintenance of a BNL are characteristic of the body of water to which it belongs, and in some instances the exact sources of the suspended material are not well known [53, 27, 69]. However, there is credible evidence for internal waves playing a role in supplying material to the BNL through local resuspension events [53, 43, 28, 54, 10].

It is worth mentioning that there are varying measures used in determining where a BNL begins. Near-bottom layers with light transmission from as high as 90% to as low as

0% have been termed as BNLs [40]. This creates a wide variability in both defining the existence of a BNL, and quantifying its thickness. A study done by Pilskaln *et al.* (2014) [49] approximated the top of the BNL in the Gulf of Maine and Bay of Fundy as the depth at which the light beam attenuation values increased by more than 40% over the overlying, mid-depth particle minimum zone. Their measurements found that BNLs of less than 5 m to 20 m thick were prevalent along the coast in water depths of less than 100 m in the area between the Scotian Shelf and eastern Jordan Basin. The average BNL thickness in the Bay of Fundy was reported to be 27 m. In another study done by Urban *et al.* (2004) [69] in the Keweenaw Peninsula of Lake Superior, the BNL was taken to be the layer where the light transmission decreased from about 85% in the clear-water zone to about 60% in the BNL. Studies performed in Lake Michigan during August 2001 [28] showed that the thickness of the BNL could vary between 0 m to 21 m in a time interval of only 20 hours, because of changes in the thermocline depth.

The composition of the material in a BNL ranges from inorganic particles (e.g. quartz and clay) to organic matter, nutrients, bacteria, plankton, and to contaminants and pollutants [23, 31, 49, 8, 44, 69]. Thus, studying and researching the potential transport of the material in the BNL through the action of ISWs could prove to be a worthwhile endeavour.

1.3 Format of Thesis

It is well known that the governing fluid equations for Environmental Fluid Dynamics (EFD) are highly nonlinear, and therefore a numerical approach is taken. As a result, the work in this thesis is based purely upon numerical simulations and is an extension of Harnanan *et al.* (2015) [24]. In this thesis, ISWs of depression and elevation propagating over bottom topography with a near-bottom stratification representing a BNL are simulated. Both two- and three-dimensional simulations are performed for the two wave-types. In the case of the wave of depression, the prograde jet at the back of the wave rolls up at the hill crest, with subsequent vortex production. In contrast, there is an entirely different instability mechanism for the wave of elevation. A gravity current develops as the wave currents carry denser fluid from the left side of the hill over to the right side. The gravity current then becomes unstable, with intense mixing at the front region. Both of these mechanisms can have implications for cross-BBL transport. Furthermore, in the depression case, there is potential for pumping finer suspended material from the BNL higher into the water column, whereas mixing of the nepheloid layer with the overlying fluid is present in the elevation case.

The structure of the remainder of the thesis is as follows. Chapter 2 covers some

background on the governing fluid equations, a brief description of the numerical model, and aspects of the theory of instability phenomena observed in this work. The model set-up and a summary of previous work [24] is given in the first section of Chapter 3. The results for both waves of depression and elevation together with a brief extension of these results to the field-scale are presented in the remainder of Chapter 3. Finally, Chapter 4 summarizes the findings of this study and future research directions are proposed.

Chapter 2

Technical Background and Methods

Due to the nonlinearity of the Navier-Stokes equations, closed form and analytic solutions do not exist except for simple situations with special symmetries, and so the numerical approach comes to the rescue. The first section of this chapter will introduce the governing equations of fluid motion, followed by a derivation of these equations under the Boussinesq approximation which results in the set of fluid equations employed in this work. Some other useful quantities and concepts in the study of fluid mechanics which are relevant to this research are also presented in this section. Internal solitary waves observed in the open oceans, lakes, and the atmosphere are nonlinear by nature [29], and so the mathematical tool for representing such waves is given in section 2.2. Next, the important features of the numerical method used for performing the numerical simulations is outlined in section 2.3.

The instabilities that occur because of BBL separation can have a large impact on sediment transport and resuspension, and cross-BBL transport [62, 24, 3, 17]: corresponding background on boundary layers is presented in section 2.4. Previous studies [62, 24, 3, 17] have shown BBL separation and associated vortex shedding in an unstratified near-bottom region to be the source of instabilities near the bottom boundary. The work in this thesis has found this to be true for an ISW of depression, even in the case of having a nepheloid layer or near-bottom stratification present. However, in the case of a wave of elevation, the density variations present in the near-bottom region caused by the near-bottom stratification have revealed a different mechanism through which mixing and cross-BBL transport may be likely to occur. The remainder of the chapter presents a brief background on some of the instability phenomena that arise in this particular instance for the wave of elevation.

2.1 Equations of Fluid Motion

It is possible to describe the motion of fluids in nature through the full set of Navier-Stokes equations: a system of nonlinear partial differential equations (PDEs). They are derived by applying Newton's second law to the fluid motion. A brief introduction to some of the important and fundamental principles in fluid mechanics will now be presented, including the Navier-Stokes equations; more details can be found in chapter 4 of Kundu [33]. The first principle is that of conservation of mass. If mass is conserved for a material volume $V(t)$ of a flowing fluid of density $\rho(\vec{x},t)$, then the following statement holds:

$$\frac{d}{dt}\iiint_{V(t)} \rho(\vec{x},t)\, dV = 0. \tag{2.1.1}$$

A material volume is the volume occupied by a fixed set of fluid particles: it is comprised of the same set of fluid particles for all time. Application of Reynolds transport theorem and the Dubois-Reymond lemma on (2.1.1) yields the conservation of mass equation:

$$\frac{\partial \rho}{\partial t} + \vec{\nabla}\cdot(\rho\vec{u}) = 0, \quad \text{or} \quad \frac{D\rho}{Dt} + \rho\vec{\nabla}\cdot\vec{u} = 0, \tag{2.1.2}$$

where $\vec{u} = \vec{u}(\vec{x},t) = (u(\vec{x},t), v(\vec{x},t), w(\vec{x},t))$ is the fluid velocity and $\frac{D}{Dt} = \frac{\partial}{\partial t} + \vec{u}\cdot\vec{\nabla}$ is the material derivative. Simply put, the material derivative gives the rate of change following a fluid particle. Equation (2.1.2) is also known as the continuity equation. A fluid is said to be incompressible if $\vec{\nabla}\cdot\vec{u} = 0$.

The next fundamental principle to be addressed is the conservation of (linear) momentum, from which the Navier-Stokes equations are obtained. Newton's second law for a fluid says that the rate of change of momentum is equal to the sum of the forces acting upon the fluid. If only body (gravity) and surface (traction) forces are taken into consideration, momentum conservation implies (after using Cauchy's stress theorem and Gauss' theorem on the traction force term):

$$\frac{d}{dt}\iiint_{V(t)} \rho\vec{u}\, dV = \iiint_{V(t)} -\rho g\hat{k}\, dV + \iiint_{V(t)} \vec{\nabla}\cdot\underline{\underline{T}}\, dV, \tag{2.1.3}$$

where g is the gravitational acceleration, and $\underline{\underline{T}}$ is the stress tensor. Note that the divergence of $\underline{\underline{T}}$ is taken row-wise. For an incompressible, Newtonian fluid (which is used in

this work), $\vec{\nabla} \cdot \underline{\underline{T}}$ simplifies to $-\vec{\nabla}p + \mu\nabla^2\vec{u}$ where $p = p(\vec{x}, t)$ is the pressure, and μ is the shear or dynamic viscosity. Similar to what was done for the conservation of mass, application of Reynolds transport theorem and the Dubois-Reymond lemma yields the desired Navier-Stokes equations (2.1.4):

$$\rho\frac{D\vec{u}}{Dt} = -\vec{\nabla}p + \mu\nabla^2\vec{u} - \rho g\hat{k}. \tag{2.1.4}$$

2.1.1 Boussinesq Approximation

In this work, an incompressible Newtonian fluid in a non-rotating reference frame under the Boussinesq and rigid-lid approximations is considered. For flows that satisfy certain conditions, the Boussinesq approximation says that the density changes in the fluid can be neglected, except where ρ is multiplied by g in the buoyancy term in (2.1.4) [33]. A quick derivation of two of the governing fluid equations under the Boussinesq equation now follows.

The density $\rho(\vec{x}, t)$ can be rewritten as $\rho(\vec{x}, t) = \rho_0 + \bar{\rho}(z) + \rho'(\vec{x}, t)$ where ρ_0 is a reference density, $\bar{\rho}(z)$ is the background density stratification, and $\rho'(\vec{x}, t)$ represents the density perturbations. A similar decomposition can be defined for the pressure, i.e. $p(\vec{x}, t) = p_0(z) + p'(\vec{x}, t)$, where $p_0(z)$ is the hydrostatic pressure profile, and $p'(\vec{x}, t)$ represents the perturbations in the pressure. Substituting these forms of the density and pressure into the momentum equation (2.1.4) in the absence of any motion ($\vec{u} = \vec{0}$) gives the hydrostatic balance condition:

$$\frac{dp_0(z)}{dz} = -\left[\rho_0 + \bar{\rho}(z)\right] g. \tag{2.1.5}$$

This condition will be used in deriving the momentum equations under the Boussinesq approximation. After substituting the above forms of the density and pressure into the momentum equation (2.1.4), dividing through by ρ_0, and simplifying using hydrostatic balance, the equation becomes:

$$\left(1 + \frac{\bar{\rho} + \rho'}{\rho_0}\right)\frac{D\vec{u}}{Dt} = -\frac{1}{\rho_0}\vec{\nabla}p' + \nu\nabla^2\vec{u} - \frac{\rho'}{\rho_0}g\hat{k} \underbrace{- \frac{1}{\rho_0}\vec{\nabla}p_0 - \frac{1}{\rho_0}\left[\rho_0 + \bar{\rho}(z)\right] g\hat{k}}_{= 0 \text{ by hydrostatic balance}}, \tag{2.1.6}$$

where the kinematic viscosity is defined by $\nu = \frac{\mu}{\rho_0}$.

The Boussinesq approximation requires that the density variations are small relative to the reference density, or in other words, $|\bar{\rho}(z)| \ll \rho_0$, and $|\rho'(\vec{x},t)| \ll |\bar{\rho}(z)|$. Thus, $1 + \frac{\bar{\rho}+\rho'}{\rho_0} \approx 1$ so that (2.1.6) reduces to

$$\frac{D\vec{u}}{Dt} = -\frac{1}{\rho_0}\vec{\nabla}p' \; + \; \nu\nabla^2\vec{u} \; - \; \frac{\rho'}{\rho_0}g\hat{k}. \tag{2.1.7}$$

However, in numerical models, it is more convenient to work with the total density and pressure fields, so adding back the hydrostatic balance terms (which are equivalent to zero) yields the desired momentum equations under the Boussinesq approximation:

$$\frac{D\vec{u}}{Dt} = -\frac{1}{\rho_0}\vec{\nabla}p \; + \; \nu\nabla^2\vec{u} \; - \; \frac{\rho}{\rho_0}g\hat{k}. \tag{2.1.8}$$

Under the Boussinesq approximation, the continuity equation (2.1.2) reduces to the incompressibility condition. This can be seen if the continuity equation is written as

$$\frac{1}{\rho}\frac{D\rho}{Dt} + \vec{\nabla}\cdot\vec{u} = 0, \tag{2.1.9}$$

since the magnitude of $\frac{1}{\rho}\frac{D\rho}{Dt}$ is small compared to the magnitudes of the velocity gradients in $\vec{\nabla}\cdot\vec{u}$ (because of the size of the density variations). The third equation (2.1.12) used in the Boussinesq approximation describes the conservation of energy for a fluid with thermal diffusivity κ. This equation is essentially the result of applying the laws of thermodynamics to the fluid, and the reader is referred to Kundu [33] for the derivation. Thus, the set of governing fluid equations used in this work are

$$\frac{D\vec{u}}{Dt} = -\frac{1}{\rho_0}\vec{\nabla}p \; + \; \nu\nabla^2\vec{u} \; - \; \frac{\rho}{\rho_0}g\hat{k}, \tag{2.1.10}$$

$$\vec{\nabla}\cdot\vec{u} = 0, \tag{2.1.11}$$

$$\frac{D\rho}{Dt} = \kappa\nabla^2\rho. \tag{2.1.12}$$

The Boussinesq approximation applies only under certain conditions. As mentioned above, the Boussinesq assumption holds only if the relative density variations are sufficiently small. Small enough density variations are ensured if the flow has a small Mach number (so that propagation of sound or shock waves is not considered, and compressibility

effects on the density are small), the vertical length scale of the flow is not too large, and the temperature and salinity differences in the fluid are small. In practice, these conditions are often met in oceanic flows, making the Boussinesq approximation a useful tool for studying such flows.

2.1.2 Buoyancy Frequency

In the study of internal waves, the Brunt-Väisälä or buoyancy frequency is an important quantity used in calculating wave solutions and properties. The buoyancy frequency, denoted $N(z)$, is the oscillation frequency of a vertically displaced fluid particle, which is released from rest in the absence of fluid friction [33]. Recall that internal waves are a result of the gravitational adjustment of vertical displacements in a stratified fluid.

A derivation of the buoyancy frequency for a fluid under the Boussinesq approximation proceeds as follows. Consider a fluid parcel of volume V at height z which is displaced upwards by a vertical distance of δ to a height of $z+\delta$. The two forces acting on this parcel are gravity, $[\rho_0 + \bar{\rho}(z)]gV$, and the buoyancy force due to the surrounding lighter fluid, $[\rho_0 + \bar{\rho}(z+\delta)]gV$. Density perturbations are ignored. If $\delta(t)$ is the displacement from the initial position, Newton's second law implies that

$$[\rho_0 + \bar{\rho}(z)]V\frac{d^2\delta}{dt^2} = [\bar{\rho}(z+\delta) - \bar{\rho}(z)]gV. \tag{2.1.13}$$

Dividing through by V and ρ_0, and using $|\bar{\rho}(z)| \ll \rho_0$, the differential equation (2.1.13) simplifies to

$$\frac{d^2\delta}{dt^2} = \frac{g}{\rho_0}[\bar{\rho}(z+\delta) - \bar{\rho}(z)]. \tag{2.1.14}$$

Finally, a Taylor expansion about z gives the equation of motion for a simple harmonic oscillator:

$$\frac{d^2\delta}{dt^2} = \frac{g}{\rho_0}\frac{d\bar{\rho}(z)}{dz}\delta, \tag{2.1.15}$$

where the square of the buoyancy frequency, $N^2(z)$, is defined as

$$N^2(z) = -\frac{g}{\rho_0}\frac{d\bar{\rho}(z)}{dz}. \tag{2.1.16}$$

A stably stratified fluid is one where the density increases with depth, i.e. $\frac{d\bar{\rho}(z)}{dz} < 0$, whereas $\frac{d\bar{\rho}(z)}{dz} > 0$ for an unstably stratified fluid and instabilities may occur. The buoyancy frequency gives a measure of the strength of the density stratification: the larger the buoyancy frequency, the stronger the stratification.

2.1.3 Vorticity

Another important equation that deals with aspects of fluid motion is the vorticity equation. Vorticity is defined as the local rate of rotation in a fluid. It is a vector field and is found by taking the curl of the velocity: $\vec{\omega} = \vec{\nabla} \times \vec{u}$. As such, if the curl of the momentum equation (2.1.10) is taken and vector identities are applied, one ends up with the vorticity equation:

$$\frac{D\vec{\omega}}{Dt} = (\vec{\omega} \cdot \vec{\nabla})\vec{u} + \nu\nabla^2\vec{\omega} - \frac{1}{\rho_0}\vec{\nabla} \times \rho g\hat{k}. \tag{2.1.17}$$

Equation (2.1.17) says that, for the fluid considered in this work, there are three possible mechanisms that can change the vorticity following the flow. The first term on the right-hand side of (2.1.17), $(\vec{\omega} \cdot \vec{\nabla})\vec{u}$, represents the rate of change of vorticity caused by tilting and stretching of vortex lines. It is not difficult to show that this term is always zero in two dimensions, indicating that there are additional sources of vorticity production/depletion in transitioning from two to three dimensions. The second term, $\nu\nabla^2\vec{\omega}$, represents the rate of change of vorticity due to molecular diffusion of vorticity, and the final term, $\frac{1}{\rho_0}\vec{\nabla} \times \rho g\hat{k}$, is the baroclinic vorticity production. This term simplifies to $\frac{g}{\rho_0}\left(\frac{\partial\rho}{\partial y}, \frac{-\partial\rho}{\partial x}, 0\right)$, which essentially says that if the density varies in the horizontal $x-y$ plane, then gravity will create a torque about the $x-y$ plane because the heavier fluid accelerates faster than the lighter fluid. Note that without the Boussinesq approximation the baroclinic vorticity production term is $1/\rho^2\left(\vec{\nabla}\rho \times \vec{\nabla}p\right)$, which means that baroclinic vorticity is generated when lines of constant density and lines of constant pressure are not parallel.

2.1.4 Reynolds Number

The Reynolds number is a crucial dimensionless quantity in fluid mechanics, which is used to help characterize flow patterns. It is defined as the ratio of the inertial forces to the viscous forces:

$$Re = \frac{UL}{\nu}. \tag{2.1.18}$$

In (2.1.18), U and L respectively represent characteristic velocity and length scales for the flow, and ν is the kinematic viscosity of the fluid. In general, small Reynolds numbers are associated with laminar flows, whereas large Reynolds numbers are more indicative of turbulent flows. The Reynolds number is an important factor in determining the physical nature of boundary layer formation, the boundary layer thickness, and possible boundary layer separation and break-down into turbulence.

When dealing with flows that involve ISWs and boundary layers, there is more than one Reynolds number that one can adopt depending on what characteristic velocity and length scale is used. Traditionally, U is chosen to be the linear long wave speed and L the fluid depth [17, 15]. However, Soontiens *et al.* (2015) [60] argue that using the linear long wave speed is incorrect, since small and large amplitude waves of the same long wave speed would have the same Reynolds number, when in fact the wave-induced currents are weaker for the smaller wave, thereby misrepresenting the actual Reynolds number. For diagnosing and predicting vortex shedding in boundary layer separation, Aghsaee *et al.* (2012) [3] have used a Reynolds number based on the momentum thickness (a measure of the boundary layer thickness; see section 2.4). The Reynolds numbers defined and used in this work are given in section 3.1.

2.2 Dubreil-Jacotin-Long (DJL) Equation

There are different mathematical theories and approaches for calculating the form of ISWs. Nonlinearity and dispersion are inherent and fundamental properties of ISWs which must be taken into account. The Korteweg-de Vries (KdV) equation is based on weakly nonlinear theory, and provides the simplest means to balance nonlinearity and dispersion. However, KdV theory is limited to describing long internal waves, where the wave is assumed to be long relative to a vertical length scale, and is of small amplitude [38]. This poses a challenge for describing and finding ISW solutions of large amplitude. Furthermore, Stastna and Lamb (2008) [62] were able to show that weakly nonlinear theory overestimates the propagation speed and underestimates the wave half-width when compared to exact, fully nonlinear ISWs.

One method for calculating exact, fully nonlinear ISWs is to use the Dubreil-Jacotin-Long (DJL) equation. The DJL equation is a single, scalar, nonlinear, elliptic eigenvalue

problem for the isopycnal displacement, $\eta(x,z)$. The DJL equation is equivalent to the full set of stratified, steady (in a reference frame moving with the wave) Euler equations, so that the computed waves are exact nonlinear solutions. The Euler equations are obtained by setting ν and κ to zero in (2.1.10) and (2.1.12). If the far upstream or background density is denoted as $\bar{\rho}(z)$, the density equation reads $\rho = \rho_0\bar{\rho}(z-\eta)$. After a long derivation (Turkington *et al.* (1991) [68]), the stratified Euler equations then reduce to the DJL equation:

$$\nabla^2\eta + \frac{N^2(z-\eta)}{c^2}\eta = 0, \tag{2.2.1}$$

$$\eta = 0 \text{ at } z = 0, -H, \tag{2.2.2}$$

$$\eta = 0 \text{ as } x \longrightarrow \pm\infty, \tag{2.2.3}$$

where

$$N^2(z) = -g\frac{d\bar{\rho}(z)}{dz} \tag{2.2.4}$$

is the square of Brunt-Väisälä or buoyancy frequency, which has been scaled by the reference denstiy ρ_0. The top of the domain is at $z = 0$, with a flat bottom at $z = -H$. The propagation speed of the wave, c, is an eigenvalue that is found as part of the solution. Once η and c are known, the wave-induced velocities can be found from the relation $\psi = c\eta$, where ψ is the streamfunction that arises because of the incompressibility condition.

For a linear stratification, $N(z)$ is constant and the DJL equation becomes linear. To the best of the author's knowledge, there are no solitary wave solutions in this case. A variational scheme was developed by Turkington *et al.* (1991) [68] to solve the DJL equation for an arbitrary density profile, which was later extended by Stastna and Lamb (2002) [61] to include background currents. In this approach, the wave amplitude is fixed by specifying the available potential energy (APE) in the wave. APE is the potential energy that is available for conversion into other forms of mechanical energy (e.g. kinetic energy), and which is ultimately available for mixing [34]. Since the DJL equation gives an exact steady-state solution to the fully nonlinear equations, it is ideally suited to be the initial condition in time-dependent, nonlinear numerical models. For the purposes of this current work, the DJL equation is solved numerically using the method in Dunphy *et al.* (2011) [19].

2.3 Numerical Methods

The DJL equation is used only for generating the initial condition for the numerical simulations in this work, because of two rather important reasons. Although the solution gives an exact, fully nonlinear ISW, the DJL equation is based on the steady-state Euler equations, meaning that there is no temporal evolution of the wave (for example as it passes over a hill). Secondly, the Euler equations are inviscid, so that dynamics and instabilities near the boundaries (where viscosity is important; see below discussion on boundary layers), which are crucial to the current work, cannot be represented. Hence, after wave initialization through the DJL equation, the Navier-Stokes equations under the Boussinesq and rigid-lid approximations are employed in the numerical methods using the numerical model SPINS.

The Spectral and Pseudo-spectral Incompressible Navier-Stokes Solver (SPINS) is software that implements a spectral collocation method for the simulation of the stratified Navier-Stokes equations under the Boussinesq approximation in three dimensions. This model was developed by Christopher Subich, a former PhD graduate (2011) and EGFD group member at the University of Waterloo. An extensive and detailed description of SPINS can be found in his PhD thesis [63], and a companion paper, Subich *et. al* (2013) [64]. The numerical accuracy of his model has been tested through several test cases. A brief account of some of the key and relevant features of SPINS is provided here.

The accurate inclusion of topography via global coordinate mapping makes SPINS an attractive and versatile numerical model. It is suitable for simulating large internal waves at the field (lake/ocean) scale, including their interaction with topography. A third-order, semi-implicit multistep method based on backwards differentiation is used for the time-discretization. The third-order method increases the accuracy, but with little additional computational cost. Modification of the time-discretization allows for variable time-steps.

In terms of the spatial discretization, the choice of both boundary conditions and domain mapping determines which spectral expansion should be used. For the configuration used in the thesis, the $z-$direction uses Chebyshev polynomials with no-slip boundary conditions at the top and bottom of the domain. Consequently, the grid points are clustered near the boundary, allowing for the resolution of boundary layer dynamics. Coordinate mapping is available if bottom topography is desired. There is more freedom of choice for the $x-$direction. A Fourier discretization can be employed for periodic, lateral boundary conditions (sine/cosine discretization for symmetric, free-slip lateral boundaries), and there is also the choice of Chebyshev polynomials for no-slip lateral boundaries.

2.4 Boundary Layers

For high Reynolds number flows, viscosity becomes important near a solid boundary since the fluid must satisfy the no-slip boundary condition at the solid surface. This region of fluid flow is referred to as a "boundary layer" (henceforth, BL). In geophysical flows in oceans and lakes, the boundary layer that forms at the bottom boundary is referred to as the bottom boundary layer (BBL). The flow velocity in the boundary layer increases away from the solid surface to match the velocity of the outer flow, and this poses the question of how to define the thickness of a boundary layer. According to Kundu [33], the three common measures of boundary layer thickness are: (1) "the $u = 0.99U$ thickness" measure, (2) displacement thickness and (3) momentum thickness.

The momentum thickness can be defined as the distance by which the boundary should be displaced in order to compensate for the loss of momentum of the actual flow because of the presence of the BL. A Reynolds number based on the momentum thickness at the separation point has been used in aerodynamics to study boundary layer instability [22, 48]. For geophysical flows, Aghsaee *et al.* (2012) [3] have used a momentum thickness Reynolds number as part of a proposed threshold criterion for vortex shedding beneath ISWs of depression propagating over both flat and sloping bottoms.

Under certain conditions, the BL flow decelerates and thickens, followed by a flow reversal and then separation. Separation, in turn, can be the source of vortices and turbulent flow. Boundary layer transition (when the flow in the BL changes from laminar to turbulent) occurs when the downstream-distance-based Reynolds number, Re_x exceeds a critical value, Re_{cr}. Since Re_{cr} varies greatly with surface shape, curvature, roughness, vibrations, and pressure gradient, predicting BL transition is a difficult task [33]. For example, $Re_{cr} \approx 10^6$ for a smooth, flat-plate BL. The key factor in producing a reverse flow is an adverse pressure gradient with respect to the flow (i.e., the pressure increases in the flow direction) [33]. The Reynolds number has a significant effect on the BL thickness, as well as the type and degree of separation, vortex production and behaviour. A higher Reynolds number means a thinner BL (the average BL thickness scales with $\frac{L}{\sqrt{Re}}$), but more turbulent separation. A "laminar separation bubble" is a feature that can occur during the separation process, whereby a laminar boundary layer separates from the surface because of an adverse pressure gradient, becomes transitional, and then the separated shear layer reattaches to the surface. It is then possible for Kelvin-Helmholtz instabilities (see section 2.5) to occur, which leads to a roll-up of the separated shear layer, forming vortex structures in the vicinity of the reattachment region [11].

2.5 Gravity Currents and Lobe-Cleft Instability

A gravity current is a primarily horizontal flow driven by gravity acting upon a fluid with horizontal variations in density. In a gravitational field, horizontal density variations produce buoyancy forces which drives flow, and these flows may be generated by a density difference of only a few percent. Gravity currents occur in both nature and man-made situations. Examples can range from thunderstorm outflows, sea breeze fronts, avalanches, underwater turbidity currents in the ocean, pyroclastic and lava flows, to spreading oil slicks and the accidental release of a (possibly poisonous) dense gas from industry. A discussion of the diversity and relevance of gravity currents can be found in Simpson [59].

A typical gravity current consists of a "head" or a frontal zone (also called "the leading edge"), followed by a tail. Shin *et al.* (2004) [58] has proposed that the speed a gravity current, U, (based on a hydraulic approach) for Boussinesq fluids in a lock-exchange set-up satisfies the following relation:

$$\frac{U}{\sqrt{g(1-\gamma)H}} = \frac{1}{2}\sqrt{\frac{D}{H}\left(2-\frac{D}{H}\right)}, \tag{2.5.1}$$

where g is the gravitational acceleration, H is the total fluid depth on both sides of the lock position, D is the height of the denser fluid, and $\gamma = \frac{\rho_1}{\rho_2} \approx 1$ is the ratio of the density of the light fluid to the density of the heavy fluid.

Although there is intense mixing in the frontal zone, a sharp dividing line between the intruding and ambient fluids is maintained. The intense mixing process has been observed in gravity currents both in the laboratory and the environment, with two main types of instabilities being responsible for the mixing: Kelvin-Helmholtz (K-H) billows and the lobe-cleft instability [59]. See Figure 2.1 for an illustration. The billows roll up in the region of velocity shear above the front of the dense fluid. A K-H instability is defined as an instability at the interface between two horizontal, parallel fluid streams of different velocities and densities (Kundu [33]). The lobe-cleft instability involves a complex shifting pattern of lobes and clefts at the head of a gravity current that moves along a horizontal boundary. It was believed that the cause of these lobes and clefts are due to the gravitational instability of the less dense fluid which is over-run by the nose of the current. However, this mechanism of lobe and cleft formation was augmented by Härtel *et al.* (2000) in two companion papers [26, 25], which demonstrated that shear plays a crucial role in the lobe-cleft formation process.

Through numerical experiments of gravity currents in the lock-exchange configuration,

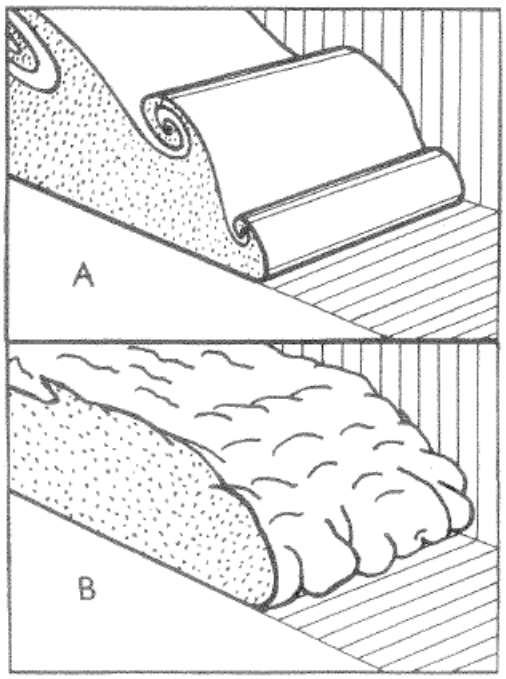

Figure 2.1: Schematic diagram of the two types of instabilities at the front of a gravity current moving along a horizontal, solid surface. Top panel: Kelvin-Helmholtz billows. Bottom panel: lobes and clefts. Source: Figure 11.3 in Simpson [59].

Härtel *et al.* attributed the lobe-cleft instability to the unstably stratified flow region between the current's nose (foremost point in the frontal region) and the stagnation point of the flow, which is located below and slightly behind the foremost part of the front. With this finding on the stagnation point location (which is different to what was previously thought where the stagnation point and the foremost point of a front coincide [59]), Härtel proposed that this creates a region of unstable stratification at the leading edge which does not involve the light fluid eventually being over-run by the front of the gravity current. They confirmed their new proposed mechanism through linear stability analysis, and showed that the amplification rate of the instability, as well as its spanwise length scale depend strongly on the Reynolds number.

2.6 Rayleigh-Taylor Instability

The Rayleigh-Taylor (R-T) is an instability that occurs when a denser fluid is placed over a lighter fluid in a gravitational field. The R-T instability has been well studied for over a century, but has become a focus for research in turbulence in recent years. R-T instabilities are quite common in nature (e.g. in oceans, supernovae and oil-trapping salt domes) and are also present in technological and industrial applications (e.g. in plasma fusion reactors). However, R-T instabilities are difficult to record because of their transient nature, and quick transition to mixing and turbulence [5].

There is a complex process associated with the development of an R-T instability. Youngs (1984) [70] categorized the development of a R-T instability into three stages, whereas Sharp (1984) [57] gave four stages. Within the past 25 years, the stages given by Youngs have been refined, and the process is still widely used in the literature today [5]. The R-T instability is a short-scale instability and its development is dependent on several factors such as the density ratio, surface tension, viscosity, compressibility and geometric constraints [57, 1].

Dalziel *et al.* (1999) [16] performed both experimental and numerical analysis of gravitationally driven mixing between salt water and fresh water. Their results indicated a qualitative difference between the 2D and 3D numerical simulations, with much more mixing occurring in the 3D case. This difference in mixing between the 2D and 3D numerical experiments has been replicated at higher resolutions by Cabot (2006) [12] and Cabot and Cook (2006) [13]. Furthermore, the authors found that the 2D flows are less well mixed, and their structural features tend to be larger in scale than their 3D counterparts at later times in the simulations.

The main scaling parameter governing the growth rate of the instability is the Atwood number [39]:

$$A = \frac{\rho_H - \rho_L}{\rho_H + \rho_L} \tag{2.6.1}$$

where ρ_H and ρ_L are the densities of the heavy and light fluids respectively. At small density differences ($A < 0.1$), up-welling of the light fluid ("bubbles") and down-welling of the heavy fluid ("spikes") form a symmetrical mixing region that expands away from the initial position of the density interface. The symmetry in the penetration of rising bubbles and falling spikes begins to be lost for an Atwood number greater than 0.5 [5].

Chapter 3

Model Set-up, Previous Work, and Results

The majority of the numerical simulations in this work were performed at the laboratory-scale with both an ISW of depression and elevation propagating over topography in the presence of a near-bottom stratification. The near-bottom stratification is used to represent a nepheloid layer, sometimes found at the bottom of lakes or oceans. This thesis was inspired by a recent publication (Harnanan *et al.* (2015) [24]), which was co-authored by the present author. The first section of this chapter presents and describes the model set-up and parameters used for the numerical simulations. Section 3.2 then proceeds to give a relevant summary of the previous work [24] driving this thesis. The laboratory-scale results are presented in the final two sections: the ISW of depression is covered first in section 3.3, followed by the ISW of elevation in section 3.4. Finally, section 3.5 presents the field-scale results for both wave-types.

3.1 Model Set-up

Both two-dimensional (2D) and three-dimensional (3D) numerical simulations were performed using a pseudo-spectral method (SPINS). The 2D simulations on experimental scales were carried out using a mapped, rectangular domain of length $L = 6$ m and height $H = 0.2$ m. The 2D simulation extended into the spanwise direction ($y-$direction), together with a perturbation, is used as the initial condition to generate the corresponding 3D simulation. The length of the domain in the spanwise direction in the 3D simulations

is $L_y = 0.1$ m. More details on initiating these simulations involving a third dimension are given in sections 3.3.2 and 3.4.2, where the 3D results are presented.

The $x-$axis runs along the top of the domain, so that the fluid surface is located at $z = 0$ m. The bottom topography consists of a single hill of amplitude 0.02 m, which is centred near the right end of the domain at $x = 5.1$ m. The equation of the bottom topography is described by the function $h(x)$, and is given in (3.1.1). The hill slope is approximately 3.5°, with the small, steepest regions being no steeper than 5°.

$$h(x) = 0.1H \operatorname{sech}^2\left(\frac{x - 5.1}{0.025L}\right) \tag{3.1.1}$$

For all of the numerical simulations in this work, periodic boundary conditions, and hence Fourier grids, were employed in the $x-$direction. In the vertical $z-$direction, no-flux and no-slip boundary conditions were applied at $z = 0$ m and $z = -H + h(x)$ m. Recall that the rigid-lid approximation is made. The use of a Chebyshev grid in the vertical allows the BBL and near-boundary dynamics to be well-resolved, since this type of grid clusters the grid points near the boundaries [64]. Fourier grids were also used in the $y-$direction for the 3D simulations.

The grid sizes for the 2D simulations are $N_x \times N_z = 2048 \times 256$, where N_x and N_z are the number of grid points in the $x-$ and $z-$directions respectively. This gives a constant grid resolution of 2.9×10^{-3} m in the $x-$direction. The vertical resolution ranges from about 2.0×10^{-4} m in the nepheloid layer to about 1.0×10^{-3} m in the centre of the water column. For the 3D simulations, the number of grid points in the spanwise is $N_y = 256$, which gives a constant grid resolution of 3.9×10^{-4} m.

A double pycnocline density stratification profile non-dimesionalized by a reference density of $\rho_0 = 10^3$ kg/m^3 (3.1.2) is used:

$$\bar{\rho}(z) = 1 - \frac{\Delta\rho_1}{2}\tanh\left(\frac{z - z_0}{d_1}\right) - \frac{\Delta\rho_2}{2}\tanh\left(\frac{z + 0.19}{d_2}\right) \tag{3.1.2}$$

The wave pycnocline is centred at $z = z_0$, where $z_0 = -0.05$ m for the wave of depression, and $z_0 = -0.15$ m for the wave of elevation. The density change and half-thickness of the wave pycnocline are given by $\Delta\rho_1 = 0.04$ and $d_1 = 0.01$ respectively. The nepheloid layer is represented by a near-bottom stratification, which has its pycnocline centred at $z = -0.19$ m. This second pycnocline is weaker and thinner, and its corresponding parameters are $\Delta\rho_2 = 0.008$ and $d_2 = 0.003$. Plots of the density profiles for the depression and elevation

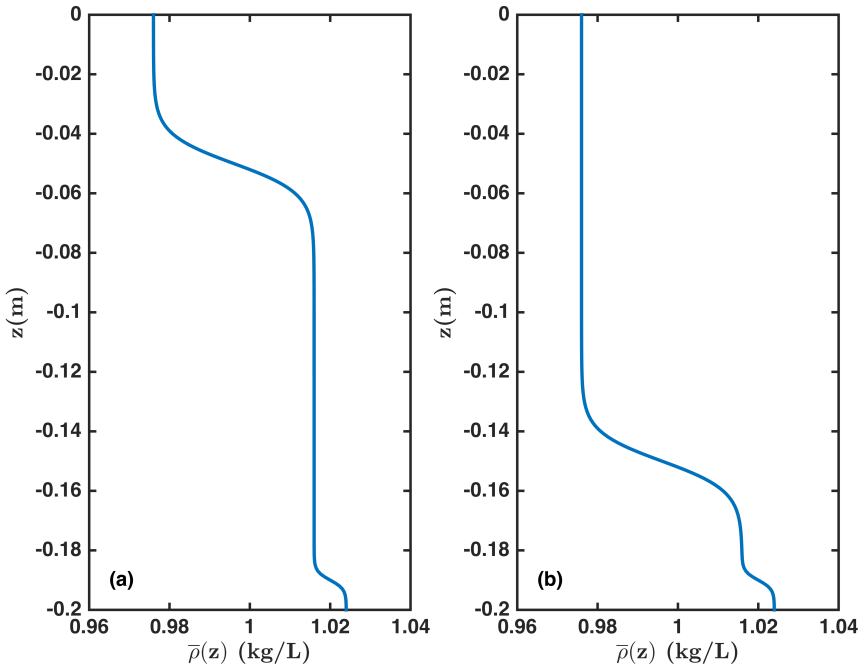

Figure 3.1: Plots of the density profile for (a) the depression and (b) the elevation simulations.

cases are given in Figure 3.1. Notice that the near-bottom pycnocline and density variations due to this pycnocline lie below the hill crest (topographic hill amplitude = 0.02 m).

The initial ISW of depression is centred at $x = 1.5$ m and the initial wave of elevation is centred at $x = 3$ m. Both waves have an amplitude of one quarter the fluid depth, or 0.05 m. The waves propagate from the left end of the domain to the right end with speed c. Figure 3.2 shows a schematic of the model set-up for the ISW of depression at time $t = 10$ s. Table 3.1 lists all of the simulations performed in this work. The wave of depression has a speed of 0.135 ms^{-1}, while the wave of elevation has a speed of 0.136 ms^{-1}. The two-layer long-wave speed for both the wave of depression and elevation are the same for this model set-up; the wave speeds scaled by the two-layer long-wave speed (1.204×10^{-1} ms^{-1}) are 1.13 and 1.12 for the wave of depression and elevation respectively. The grid and domain parameters are also included in Table 3.1. Table 3.2 lists the physical parameters used in the simulations.

The Reynolds number based on the maximum wave-induced current below the wave

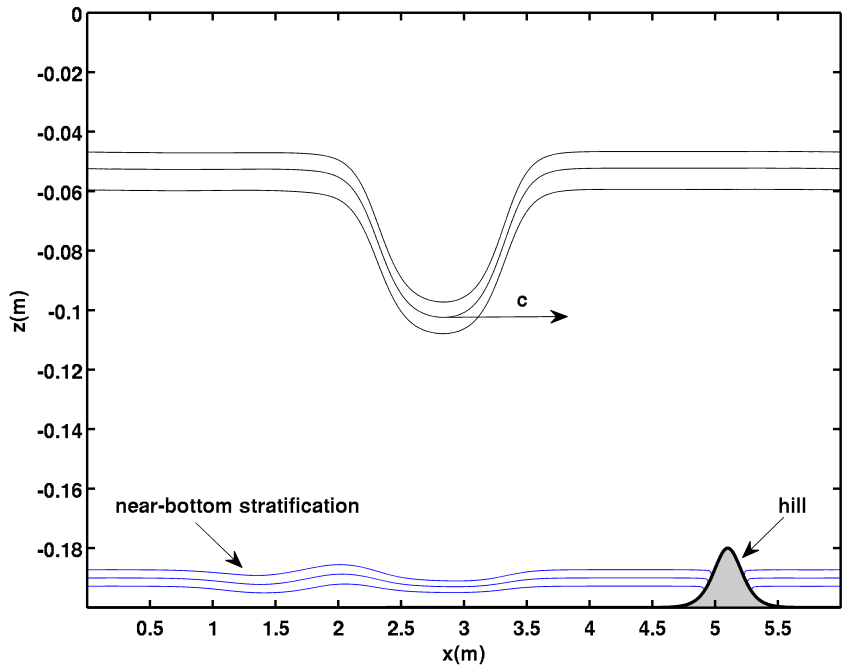

Figure 3.2: A schematic diagram of the model set-up for a simulation with the ISW of depression. The wave pycnocline is centred at $z = -0.05$ m and the wave propagates from the left to the right with speed c. The weaker and thinner near-bottom pycnocline is centred at $z = -0.19$ m. The topographic hill of amplitude 0.02 m is centred at $x = 5.1$ m.

pycnocline and at the top of the nepheloid layer is:

$$Re_w = \frac{u_{max} H}{\nu} \approx 1.4 \times 10^4 \tag{3.1.3}$$

This Reynolds number is quite large as it uses the entire fluid depth to be the typical length scale. It is possible to quote a jet-based Reynolds number [24] using the velocities and vertical extent of the prograde jet behind the ISW of depression, both of which are smaller:

$$Re_{jet} = \frac{u_{jet} H_{jet}}{\nu} \approx 300 \tag{3.1.4}$$

It can also be of interest to quote a Reynolds number based on the nepheloid layer. The nepheloid layer is approximately the same thickness as the fully developed jet behind the ISW. Therefore, if the velocity of the jet is used in the case of an ISW of depression, the Reynolds number would be $Re_{nepheloid} = Re_{jet}$. If the wave-induced currents in the nepheloid layer are taken as the typical velocity scale, then $Re_{nepheloid} \approx 700$.

Table 3.1: Grid and domain parameters for the different simulations.

Case Label	N_x	N_y	N_z	L (m)	H (m)	L_y (m)
Wave of depression	2048	N/A	256	6	0.2	N/A
Wave of depression 3D large noise	2048	256	256	6	0.2	0.1
Wave of depression 3D small noise	2048	256	256	6	0.2	0.1
Wave of depression dye	2048	N/A	256	6	0.2	N/A
Wave of depression dye 3D	2048	256	256	6	0.2	0.1
Wave of elevation	2048	N/A	256	6	0.2	N/A
Wave of elevation 3D large noise	2048	256	256	6	0.2	0.1
Wave of elevation 3D small noise	2048	256	256	6	0.2	0.1
Wave of elevation dye	2048	N/A	256	6	0.2	N/A
Wave of elevation dye 3D	2048	256	256	6	0.2	0.1

Table 3.2: Physical parameters for the simulations.

Physical parameter	Bottom-stratified simulations	Dye simulations
Gravitational acceleration, g (m/s^2)	9.81	9.81
Viscosity, ν (m^2/s)	1×10^{-6}	1×10^{-6}
Thermal diffusivity, κ (m^2/s)	5×10^{-7}	5×10^{-7}
Dye diffusivity, κ_{dye} (m^2/s)	N/A	5×10^{-7}

3.2 Previous Work

The work given in this thesis was inspired and motivated by the results of work published in January, 2015 (Harnanan *et al.* [24]). This article, entitled "Internal wave boundary layer interaction: A novel instability over broad topography", presented a new type of bottom boundary layer (BBL) instability that occurs for an ISW of depression propagating over broad, gently sloping topography. This section of the thesis will summarize the important

and relevant results of [24], so that the reader can better follow and appreciate the work in this thesis.

The numerical method employed in [24], SPINS, is identical to that used in the present work. However, the model set-up differs in a number of ways. Firstly, Harnanan *et al.* did not consider a near-bottom stratification. There was a single pycnocline, which provided the waveguide for the ISW of elevation or depression: the density profile is given in equation 3.2.1. The waves of depression and elevation were extreme, in that the widths of the waves were about 3.4 m, which is almost 1.9 times the width of the waves in the present work. However, their amplitudes were the same as those used here, i.e. 25% of the water column, making the available potential energy (APE) of the previous wave three times larger than the APE of the present waves. The bottom topography of [24] was comprised of two topographic hills (see (3.2.2)) instead of just one, and they were marginally less steep (slope of about 2.5°) than the hill used for this thesis. As a result, the domain was twice as long in the $x-$ direction, but the grid resolution used in the horizontal was the same as the present horizontal grid resolution. See panel (a) of Figure 3.3 for an idea of the experimental set-up. The fluid depth and vertical resolutions were the same in both works. However, the 3D simulations in the present work possess superior resolution in the spanwise direction: 3.9×10^{-4} m compared to 2.1×10^{-3} m in [24].

$$\bar{\rho}(z) = 1 - 0.02 \tanh\left(\frac{z + 0.05}{0.01}\right) \tag{3.2.1}$$

$$h(x) = 0.02\left(\operatorname{sech}^2\left(\frac{x - 9}{0.3}\right) + \operatorname{sech}^2\left(\frac{x - 10.2}{0.3}\right)\right) \tag{3.2.2}$$

Both ISWs of depression and elevation were considered in [24], and propagated over both narrow (slope of 8°) and broad (slope of 2.5°) hill topography. The topography was quite gentle when compared to previous studies such as Maderich *et al.* (2010) [42] and Talipova *et al.* (2013) [65], which considered ISWs propagating over step-like topography. The practicality and hence applicability of these two studies with a bottom step may, however, be somewhat limited in attempting to describe ISW interaction with topography in lakes or the ocean. There are many topographic features in the ocean that have gentle slopes, such as large-scale sills, which have slopes ranging from 0.2° to 8.5° (See Table 1 of Ref. [7]). Continental slopes in the ocean also have average slopes of 3° or 4° [6, 50, 14]. On smaller scales, sand waves [67, 4] and mud waves [20] typically have slopes of less than 3°.

For the wave of elevation, only some minor separation with no subsequent vortex production was observed in the BBL for the case of the broad hill. In the case of the narrow

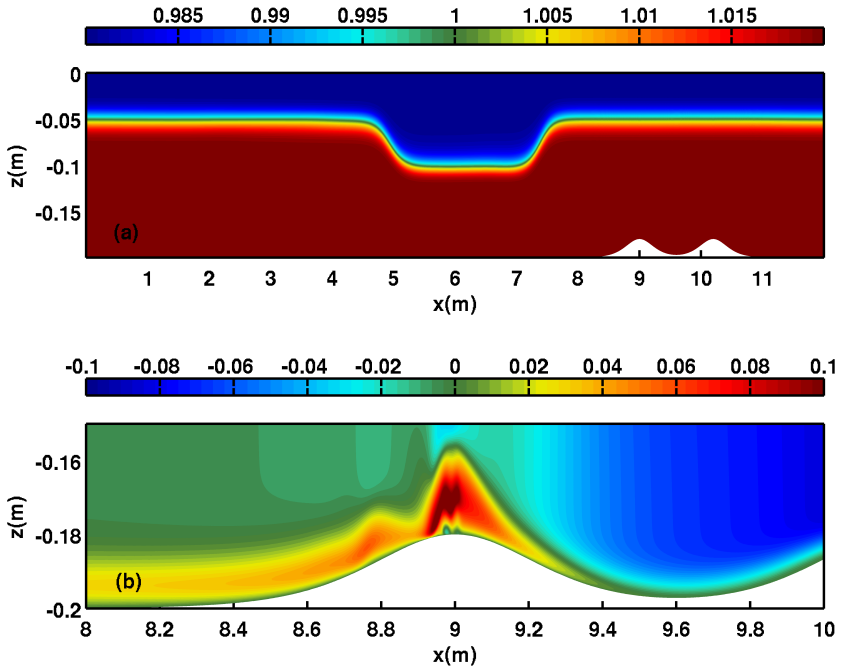

Figure 3.3: Simulations from Harnanan *et al.* (2015). Panel (a) shows the basic set-up for the ISW of depression at $t = 24$ s before the wave reaches the hills. The density is saturated between 0.98 kg/L and 1.02 kg/L. Panel (b) shows the horizontal velocity field at $t = 57$ s, when the jet rolls up as it reaches the hill crest. The horizontal velocity is saturated at 0.1 ms^{-1}.

topography, significant overturns in the wave pycnocline were present, in addition to BBL separation and associated vortex production.

With the ISW of depression, a novel instability was observed as the wave passes over the broad topography. The broad hill was too gentle to induce separation, but the prograde jet at the back of the wave (a feature of ISWs of depression; see panel (b) of Figure 3.4 for a visualization) accelerated as it crept up the hill slope, and then rolled up at the hill crest as shown in panel (b) of Figure 3.3. The jet roll-up evolved into vortex production; the mechanism for this instability is given in section III, part A of [24]. However, the narrow hill was steep enough to induce BBL separation, and consequently vortex production during the wave's passage over the hill. It was found that the bottom shear stress for the case of the broad topography only became significant after the wave had passed the hill crest,

which indicated that the jet roll-up instability was responsible.

For the wave of depression, the jet roll-up and separation instabilities were compared in detail. The results concluded that although the jet roll-up instability yielded small amounts of three-dimensionalization, it provided an efficient means of pumping material out of the BBL in a large geographical area. The separation instability yielded more vigorous three-dimensionalization in a smaller geographical area compared to the jet roll-up instability, but the magnitude of the pumping was comparable. It is important to note that for the purposes of quantifying the degree of three-dimensionalization in [24], the spanwise standard deviation of kinetic energy scaled by the maximum kinetic energy was used. Heuristic values of 0.01 were taken to indicate moderate 3D flow, whereas a value of 0.2 indicated that three-dimensionalization was important. This measure for assessing the degree of three-dimensionalization will be employed in the thesis.

In the present work, a broad hill as in [24] was chosen, since the author postulates that the classical BBL separation instability would occur for the narrow hill in the presence of a nepheloid layer (provided reasonable assumptions hold, for example, the wave is energetic and large enough). Although the wave used in this work is narrower with one third the APE of the wave in [24], only the energetics and physical size of the instabilities are expected to deviate slightly. The smaller wavelength of the present ISW, together with the fact that only one hill is used, allows for a smaller domain which saves on the computational cost and allows for improved resolution in the spanwise direction.

3.3 Internal Solitary Wave of Depression

ISWs of depression are the most common types of mode-1 ISWs observed in the the open ocean and lakes. This section presents the results for the simulations involving the ISW of depression: the first five cases in Table 3.1. The first subsection discusses the 2D results, while the second subsection covers the 3D results. Comparisons between the simulations with the nepheloid layer, referred to as the 'bottom-stratified' simulations, and those with the passive tracer, referred to as the 'dye' simulations, are made in each subsection. Both the bottom-stratified and dye simulations exhibit a jet roll-up at the hill crest with subsequent vortex production. The vortex structures in the nepheloid layer case are smaller and less energetic than those in an unstratified bottom, making them less efficient at cross-BBL transport. Nevertheless, there is still potential for transport of the suspended material in the BNL higher into the water column.

3.3.1 Two-dimensional Simulations

Two simulations performed in two dimensions with the ISW of depression are discussed: a bottom-stratified simulation and a dye simulation. These are chosen from a larger, exploratory set of simulations. The dye acts as a passive tracer and enabled the author to track the dynamics in the near-bottom region of the domain in the absence of a nepheloid layer. The dye field had the same spatial structure as the nepheloid layer and was saved separately. The diffusivity of the dye was set to be the same as that of the fluid and the gravitational acceleration acting on the dye was set to zero so that the dye was indeed a passive tracer. The intended goal of the dye simulation was to examine how the presence of a nepheloid layer affects the instabilities in the near-bottom region when compared to an unstratified bottom. In the dye simulation, the dye field 'tracks' the fluid in the near-bottom region that would correspond to the fluid in the nepheloid layer for the bottom-stratified simulation.

Before any actual results are reported, the general structure and features of an ISW of depression are briefly mentioned. An ISW generates wave-induced currents which depend on the polarity of the wave, i.e. elevation or depression. Panel (a) of Figure 3.4 shows the wave of depression used in this work as seen through the density field at $t = 11$ s for the bottom-stratified simulation. Recall that the wave propagates from left to right. The reader can notice that the true aspect ratio of the domain (≈ 0.033) is not reflected in these plots, as the vertical length scale in the plots is much smaller than the horizontal length scale.

The horizontal wave-induced currents are shown in panel (b). The currents are positive above the wave trough and negative below. They are strongest directly above/below the centre region of the wave and decrease in magnitude outwards. When the no-slip boundary condition is enforced, ISWs of depression exhibit a feature called a "prograde jet", which is a thin layer of fluid that exists at the back of the main wave body. The jet travels along the bottom boundary in the direction of wave propagation. The velocities associated with the jet are considerably smaller in magnitude than those in the wave footprint. For the present wave, the typical wave-induced currents are about 0.06 ms^{-1} in magnitude, whereas the typical velocity of the jet is around 0.02 ms^{-1}. The vertical wave-induced currents for an ISW of depression are downward in the front half region of the wave, and upward in the rear half region, as illustrated in panel (c) of 3.4. The wave shown has typical vertical currents of 0.01 ms^{-1} in magnitude.

Figure 3.5 shows an overview of the ISW of depression passing over the hill in the bottom-stratified run. Passage over the topography creates a small imprint on the body of the wave, while the wave-induced currents create a region of lighter fluid in the nepheloid

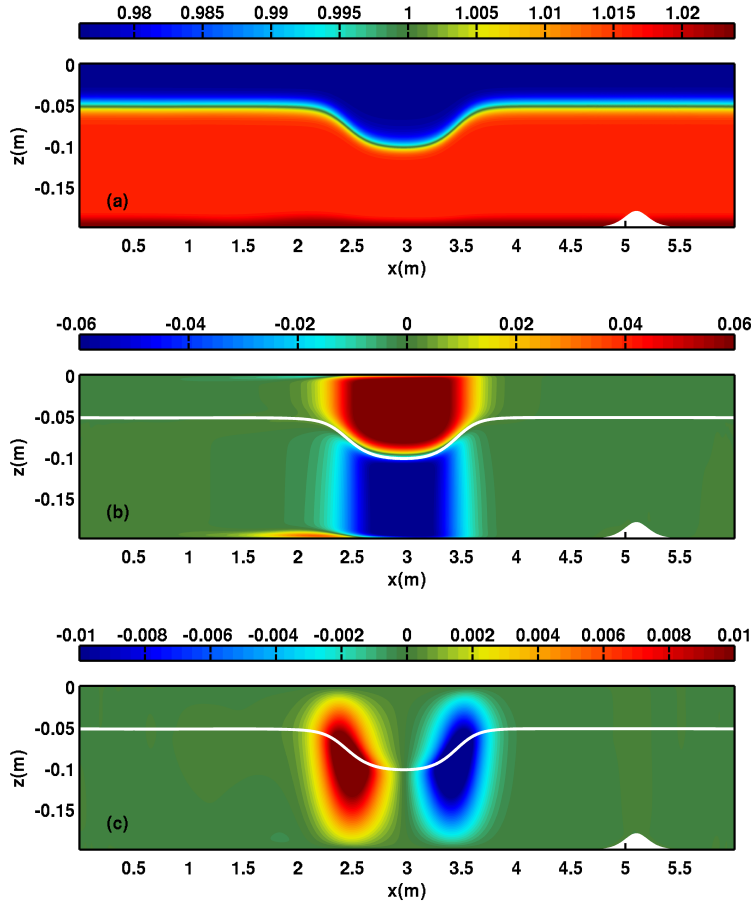

Figure 3.4: ISW of depression with near-bottom stratification. The wave and its currents are shown for time $t = 11$ s before the wave reaches the hill. The entire computational domain is shown. (a) Density plot saturated between 0.976 kg/L and 1.0238 kg/L. The pycnocline of the near-bottom stratification lies below the hill crest. (b) Horizontal velocity saturated at 0.06 ms^{-1}. (c) Vertical velocity saturated at 0.01 ms^{-1}. The white density contours in panels (b) and (c) correspond to a density of 1 kg/L.

layer. This is because the nepheloid layer lies below the hill crest, so that the hill separates this region of denser fluid on either side of itself. In panel (a), the wave centre is just before the hill crest at $t = 26$ s, and so the imprint caused in the nepheloid layer creates a momentary void of dense fluid on the left side of the hill at this time. In comparison, the distortion of the wave pycnocline is negligible.

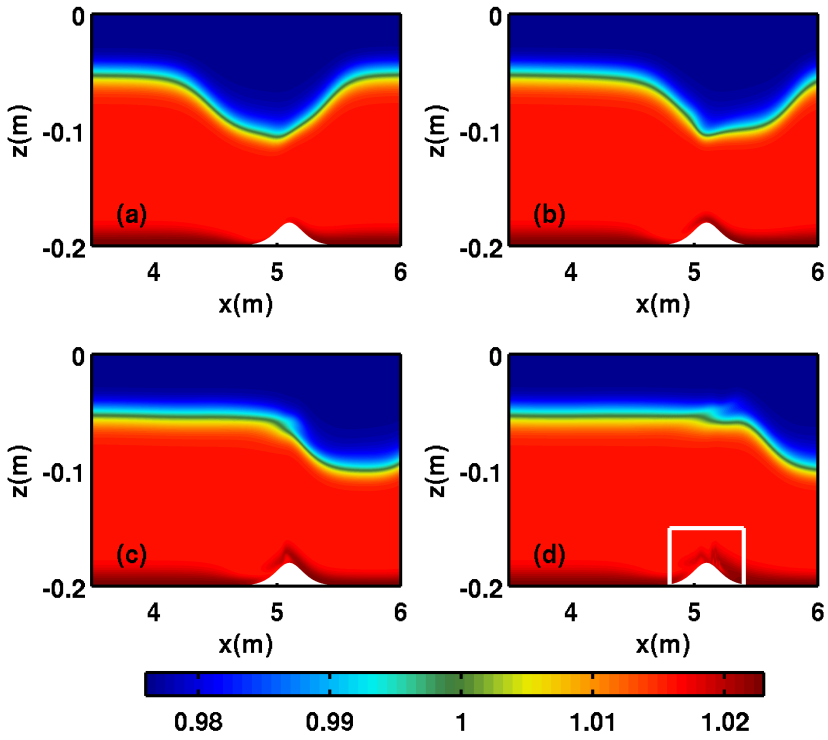

Figure 3.5: Density plots of the ISW of depression for the bottom stratified case as it propagates over the hill. (a) $t = 26$ s, (b) $t = 29$ s, (c) $t = 32$ s, (d) $t = 35$ s. The density is saturated between 0.976 kg/L and 1.023 kg/L. The white box in panel (d) shows the portion of the domain that Figure 3.7 zooms in on.

A few seconds later at $t = 29$ s the wave is more deformed and the denser fluid in the nepheloid layer on the right side of the hill has begun to creep up the right slope of the hill, over the hill crest, and onto the left side, as shown in panel (b) of Figure 3.5. This is due to the action of the horizontal wave-induced currents. Panels (a) and (b) of Figure 3.6 zoom in on the density and horizontal fields respectively at $t = 29$ s to offer an explanation. At this point, the prograde jet has arrived at the foot of the hill and is beginning to make its way up the hill. It is interesting to observe from the panels of Figure 3.6 that as the jet moves along with the wave, it will at times consist of both the denser fluid in the nepheloid layer and the overlying lighter fluid (for example, see panels (c) and (d)), or only the fluid

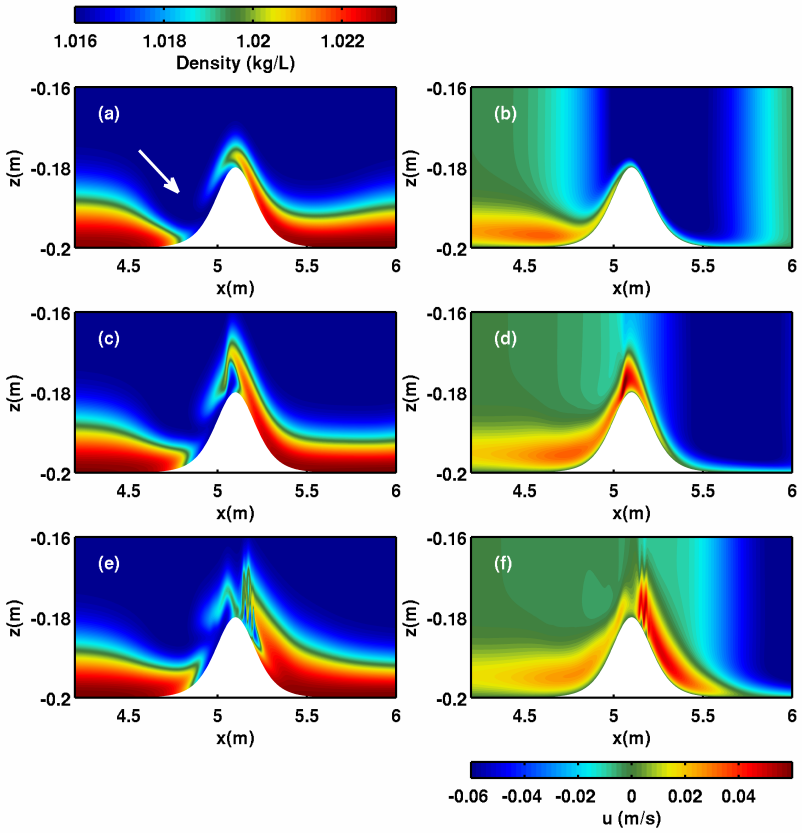

Figure 3.6: A closer look at the density and horizontal velocity fields as the wave progresses over the hill. The left panels are density plots saturated between 1.016 kg/L and 1.023 kg/L, and the right panels are horizontal velocity plots saturated at 0.06 ms^{-1}. Panels (a) and (b) are at $t = 29$ s, (c) and (d) are at $t = 32$s, (e) and (f) are at $t = 35$ s. The white arrow in (a) points to the region where there is no density stratification because of the hill.

in the nepheloid layer (for example, at an earlier time before the jet reaches the hill).

Further progression of the wave over the hill at $t = 32$ s sees the denser fluid moving farther leftward over the hill and rising upward at the hill crest, as illustrated in panel (c) of Figure 3.5. The elevation of the dense fluid at the hill crest coincides with the acceleration of the jet head, which is responsible for the motion. Refer to panels (c) and (d) of Figure 3.6 for a closer look at the density and horizontal velocity fields respectively at $t = 32$ s. The wave has recovered its original shape at this time, except for a small

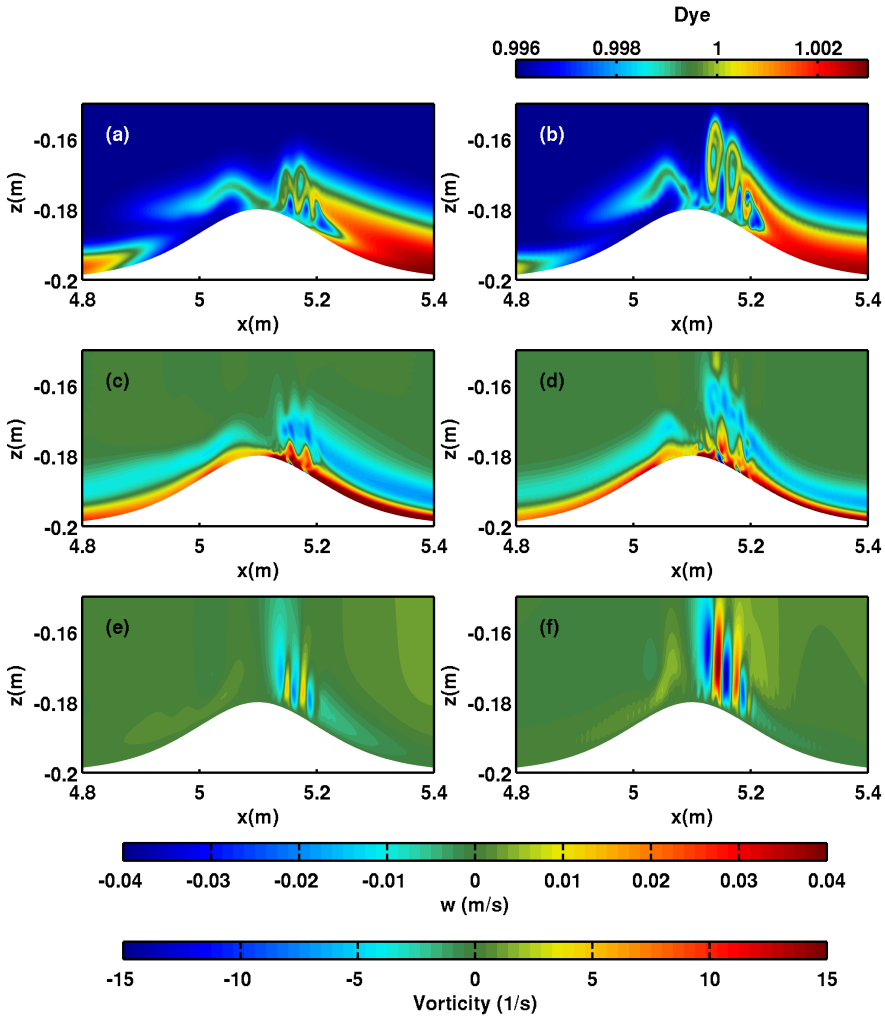

Figure 3.7: Comparison with the dye simulation at $t = 35$ s. The instability region is zoomed in on. (a) density plot saturated between 1.016 kg/L and 1.023 kg/L as in Figure 3.6. (b) dye plot saturated between 0.996 and 1.003. (c) and (d) are vorticity plots for the bottom-stratified and dye cases, respectively. Vorticity plots are saturated at 15 s^{-1}. (e) and (f) are vertical velocity plots for the bottom-stratified and dye cases, respectively. Velocity plots are saturated at 0.04 ms^{-1}.

disturbance in the pycnocline at the back-end of the wave.

Three seconds later at $t = 35$ s, vortex production has occurred in the nepheloid layer on the right side of the hill close to the hill crest, as shown in panel (d) of Figure 3.5. This is

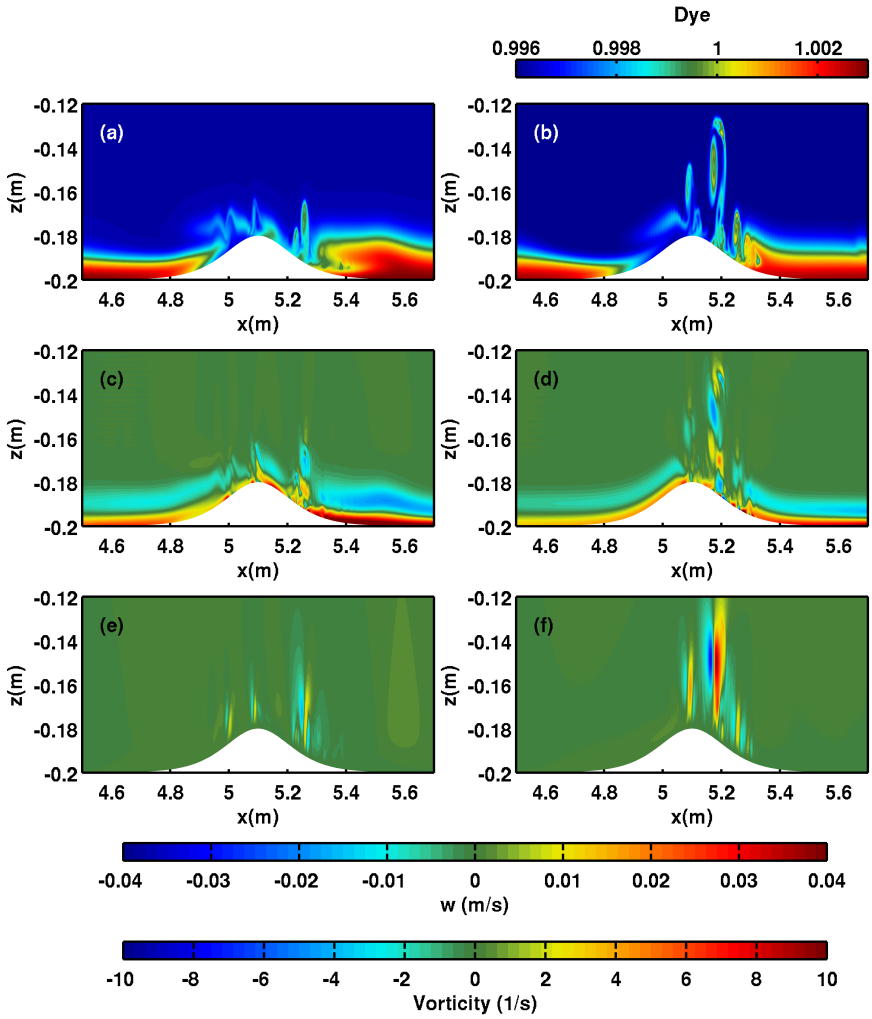

Figure 3.8: Comparison with the dye simulation at $t = 40$ s. The instability region is zoomed in on. (a) density plot saturated between 1.016 kg/L and 1.023 kg/L as in Figure 3.6. (b) dye plot saturated between 0.996 and 1.003. (c) and (d) are vorticity plots for the bottom-stratified and dye cases, respectively. Vorticity plots are saturated at 10 s^{-1}. (e) and (f) are vertical velocity plots for the bottom-stratified and dye cases, respectively. Velocity plots are saturated at 0.04 ms^{-1}.

as a result of the jet rolling up, an instability which is of the same nature as that discussed in Harnanan *et al.* [24]. See panels (e) and (f) of Figure 3.6 for a more detailed illustration. Disturbances in the wave pycnocline are still not very significant. To determine how this

instability would differ in the absence of the nepheloid layer, comparisons are made to the dye simulation.

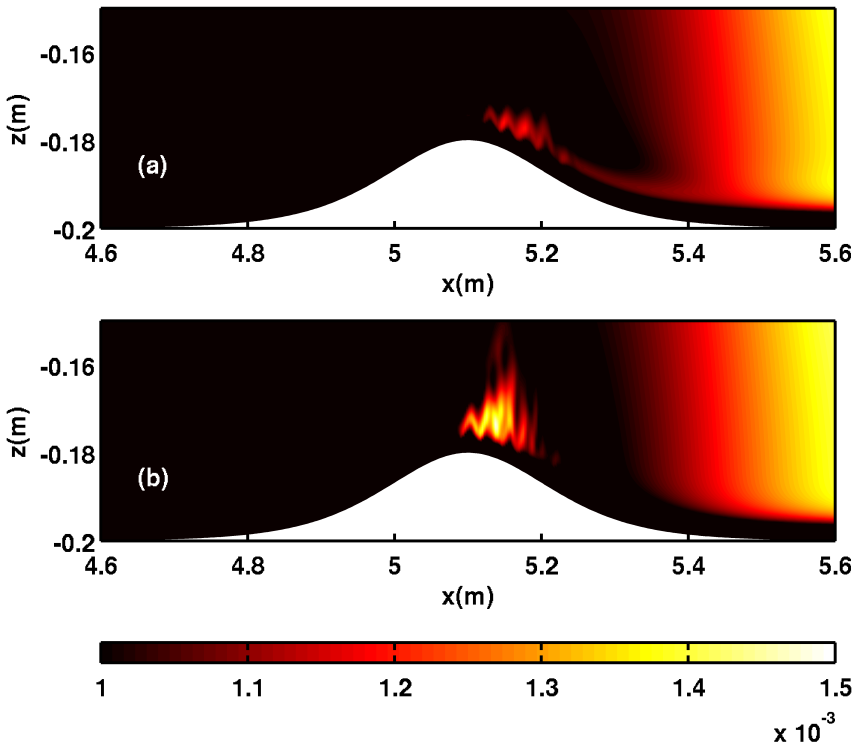

Figure 3.9: Kinetic energy averaged over time period $t = 29$ s to $t = 36$ s. (a) Stratified case, (b) Dye case. The kinetic energy is saturated between 41.7% and 62.5% of the maximum.

Figures 3.7 and 3.8 follow the same format, and compare the bottom-stratified simulations with the dye simulations at $t = 35$ s and $t = 40$ s respectively. Panels (a), (c) and (e) are the density, vorticity and vertical velocity fields for the bottom-stratified simulations respectively, whereas panels (b), (d) and (e) show the corresponding fields for the dye simulations, with panel (b) showing the dye field instead. At $t = 35$ s the instability region extends higher into the water column for the dye simulation, about 0.01 m higher. The vortices are also more defined and larger when compared to the bottom-stratified run: this is illustrated in the density/dye and vorticity plots. We reason that this difference is because more energy has to be put into lifting the denser fluid in the near-bottom stratification. However, the vorticity magnitude is comparable for the two cases at this time,

even though the vertical velocities are not. The magnitude of the vertical velocities in the instability region for the bottom-stratified case ranges from about 0.01 ms^{-1} to 0.02 ms^{-1}, whereas for the dye case these velocities range from about 0.03 ms^{-1} to 0.04 ms^{-1} (which is at least double in size). The stronger vertical velocities present in the instabilities that extend higher into the fluid column would suggest that an unstratified bottom would be more efficient at pumping material out of the BBL and BNL and transporting it higher into the water column. This inference, however, needs to be confirmed in a 3D simulation.

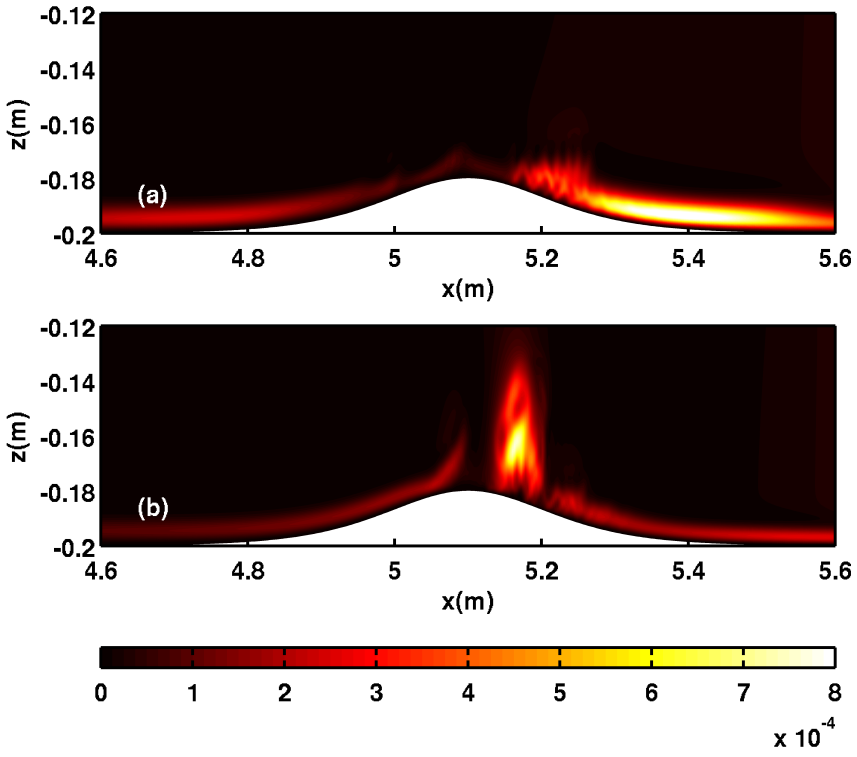

Figure 3.10: Kinetic energy averaged over time period $t = 36$ s to $t = 40$ s. (a) Stratified case, (b) Dye case. The kinetic energy is saturated between 0% and 28.6% of the maximum.

The difference in the evolution of the instabilities for the bottom-stratified and dye cases is shown at a later time ($t = 40$ s) in Figure 3.8. At this time, the vortices for the bottom-stratified run have weakened and are confined to the near-hill region. However, in the dye case the vortices have separated and travelled up the water column a significant distance, about 0.07 m from the domain bottom, although they have also weakened. The

vertical velocities for the dye case are still much stronger than the bottom-stratified case (about three times stronger).

In view of the difference in the instabilities and energetics for the bottom-stratified and dye cases, plots of the time-averaged kinetic energy were made. Figure 3.9 shows plots of the kinetic energy averaged over the time interval from $t = 29$ s to $t = 36$ s. For this time interval, the kinetic energy in the instability region for the dye case is approximately 1.2 times greater than that of the bottom-stratified case. In other words, this says that the instability region for the bottom-stratified case is less energetic, as more of the energy goes into lifting the heavier fluid. Similar plots in Figure 3.10 show the time-averaged kinetic energy for the interval $t = 36$ s to $t = 40$ s. It is interesting to note that at later times, most of the kinetic energy for the bottom-stratified run is concentrated along the boundary where there is little influence of vortices. This can indicate the possibility of three-dimensionalization in that region, and this claim is confirmed in the next section. In contrast, the kinetic energy remains localized to the instability vortex region in the dye simulation.

3.3.2 Three-dimensional Simulations

The significant upward transport of dye into the water column shown in Figure 3.8, approximately 0.08 m from the bottom, indicates that ISWs moving over an unstratified bottom domain would, in the right circumstances be highly efficient at transporting and re-circulating material a considerable height into the water column. Of course, this hypothesis needs to be confirmed in a 3D simulation, and indeed it was found to be the case.

In initializing a 3D simulation, the 2D simulation extended into the spanwise dimension is used as the initial condition. A white noise perturbation is used to seed any spanwise instabilities, and hence no spanwise mode is forced preferentially. In this section, the effect of the noise amplitude is investigated for the ISW of deperession propagating over a hill with a near-bottom stratification. The motivation for exploring different noise amplitudes is to consider the size of these perturbations, since finite perturbations would dominate in the field.

Two 3D simulations were run, with the perturbation sizes differing by two orders of magnitude. The larger perturbation was chosen to be the conventional magnitude: 1% of the absolute value of the maximum velocity in the 2D run at the time when the 3D run was initialized. This value was 1.0×10^{-3}, and the smaller perturbation simulation used a noise amplitude of 1.0×10^{-5} ms^{-1}. The dye simulation was also extended into the third

dimension and used the conventional perturbation magnitude as in the large noise run (1.0×10^{-3} ms^{-1}). These three simulations were initialized at time $t = 28$ s, when the ISW has just arrived at the hill and begins to interact with the hill. Panel (b) of Figure 3.5 can be used to gauge where the wave is at $t = 28$ s. The 2D simulations saved the data fields every second, while the 3D simulations saved the data fields at a shorter time interval of 0.25 seconds. The results are now presented and discussed.

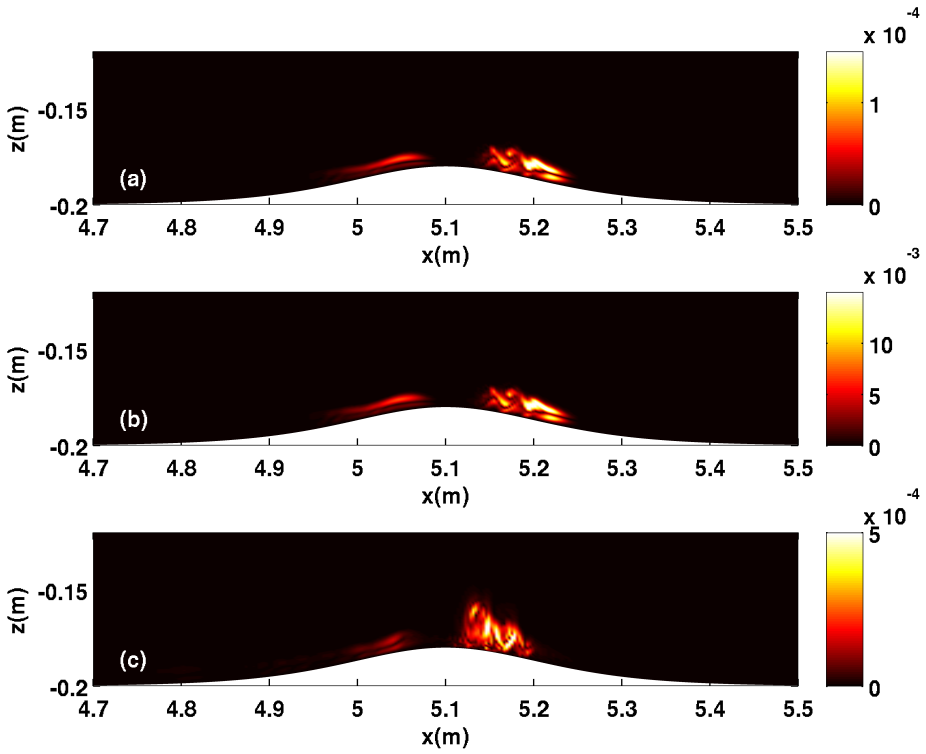

Figure 3.11: Plots of the spanwise standard deviation of kinetic energy scaled by the maximum kinetic energy for time $t = 35$ s. (a) small perturbation simulation (b) large perturbation simulation (c) dye simulation. Only the instability region is shown.

The spanwise standard deviation of kinetic energy scaled by the maximum kinetic energy is used to estimate the degree of three-dimensionalization (refer to section 3.2). Figures 3.11 and 3.12 show plots of this quantity for the three different simulations at times $t = 35$ s and $t = 40$ s respectively. Examination of these figures allows for the following comparisons and deductions to be made. Although the scaled spanwise standard deviation

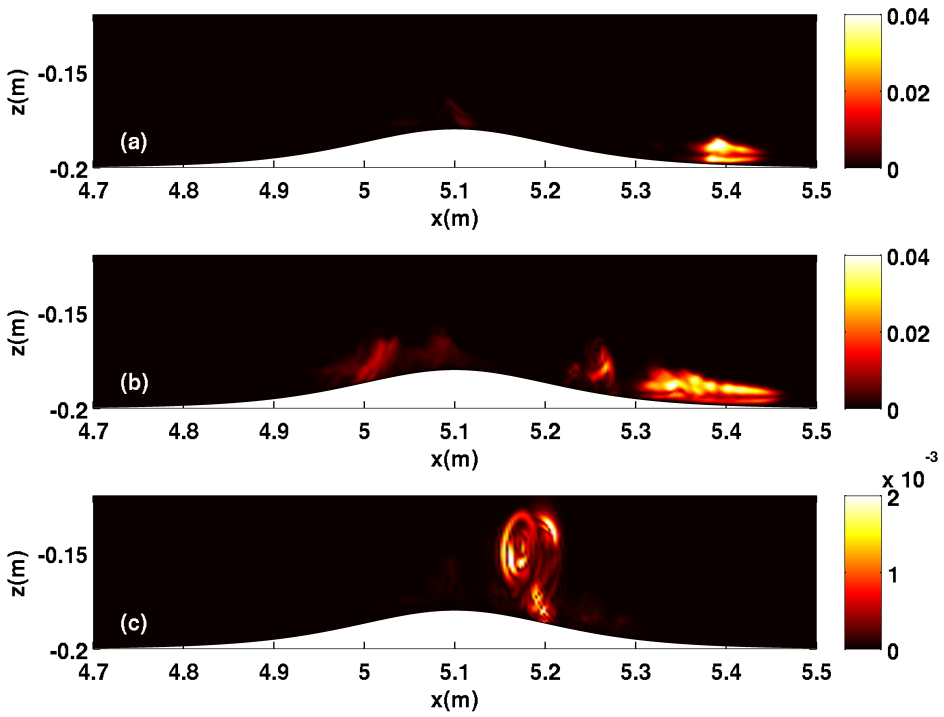

Figure 3.12: Plots of the spanwise standard deviation of kinetic energy scaled by the maximum kinetic energy for time $t = 40$ s. (a) small perturbation simulation (b) large perturbation simulation (c) dye simulation. Only the instability region is shown. Note the colorbar change for the dye simulation.

of kinetic energy increases by a factor of approximately 250 for the small perturbation case from $t = 35$ s to $t = 40$ s, the flow is only moderately 3D (maximum value of about 0.04) at the latter time. The size of the instability region stays roughly the same through this five second window and has shifted rightward along the boundary to the foot of the hill.

In the case of the large noise simulation, the scaled spanwise standard deviation of kinetic energy has approximately doubled from $t = 35$ s to $t = 40$ s. Comparing this increase to the corresponding small noise case, it is very easy for the reader to validate his/her speculation that three-dimensionalization sets in quicker for the large noise run. Note that the degree of three-dimensionalization reaches a limit in each simulation. Observe that though the spatial extent of the three-dimensionalization region is the same at $t = 35$

s for both the small and large noise cases, the instability region has grown much more for the large noise run at $t = 40$ s. However, the degree of three-dimensionalization for the large noise case is also only moderate (maximum value of no more than 0.04). The region containing the 3D structure is localised near the boundary from about $x = 5.3$ m to $x = 5.45$ m in panel (b) of Figure 3.12, and coincides with part of the region of highest kinetic energy in panel (b) of Figure 3.10.

Finally, for the dye simulation, both the 3D instability (vortex) region and scaled spanwise standard deviation of kinetic energy have grown from $t = 35$ s to $t = 40$ s, as observed in the large perturbation case. However, even at $t = 40$ s the scaled spanwise standard deviation of kinetic energy is only about 0.002, approximately 20 times smaller than the large perturbation case, which indicates that three-dimensionalization is nearly insignificant. Calculations at 41.5 s (not shown), when the wave crest is at 6.9 m (and the rear of the wave is at approximately $x = 6$ m), reveal that the scaled spanwise standard deviation of kinetic energy is always less than 0.005. This is in contrast to the wave of depression in Harnanan *et al.* [24] where moderate three-dimensionalization was achieved. This difference can be attributed to the more energetic wave and prograde jet in [24].

In order to get an idea of the form and spatial distribution of the 3D structure, $x - y$ slices of the spanwise and vertical velocity fields were made. These plots were done at $t = 40$ s when the instabilities are fully developed and the flow is moderately 3D (refer to the discussion of Figures 3.11 and 3.12 above), and they are presented in Figures 3.13 and 3.14 respectively. The black contours are chosen to be near the boundary, not only because we are chiefly interested in the near-bottom dynamics, but simply because the instabilities for the bottom-stratified simulation are localized to the near-bottom region. The black contours are at a height of approximately 0.01 m above the topography, which coincides with the centre of the near-bottom pycnocline.

The left panels of Figure 3.13 are in agreement with the 2D simulations, in that the instabilities in an unstratified near-bottom domain would produce stronger pumping of material out of the BBL a considerable distance into the water column when compared to a BNL being present. The typical vertical velocities in the instability region at this time are very similar for the small and large perturbation cases, approximately 0.01 ms^{-1} in magnitude, whereas the dye simulation velocities are about $0.02 - 0.03$ ms^{-1} in the large vortex region at $x = 5.16$ m, suggesting that an unstratified near-bottom does indeed have much greater potential for pumping of material. Empirical evidence suggests that a sufficient bottom shear stress is required to induce incipient sediment motion at the bed before sediment resuspension can occur; this is assessed using the Shields parameter [47, 2, 21, 45, 46]. Although the vertical velocities are significant for the unstratified case, a high enough bed shear stress is needed to resuspend sediment that rests on the

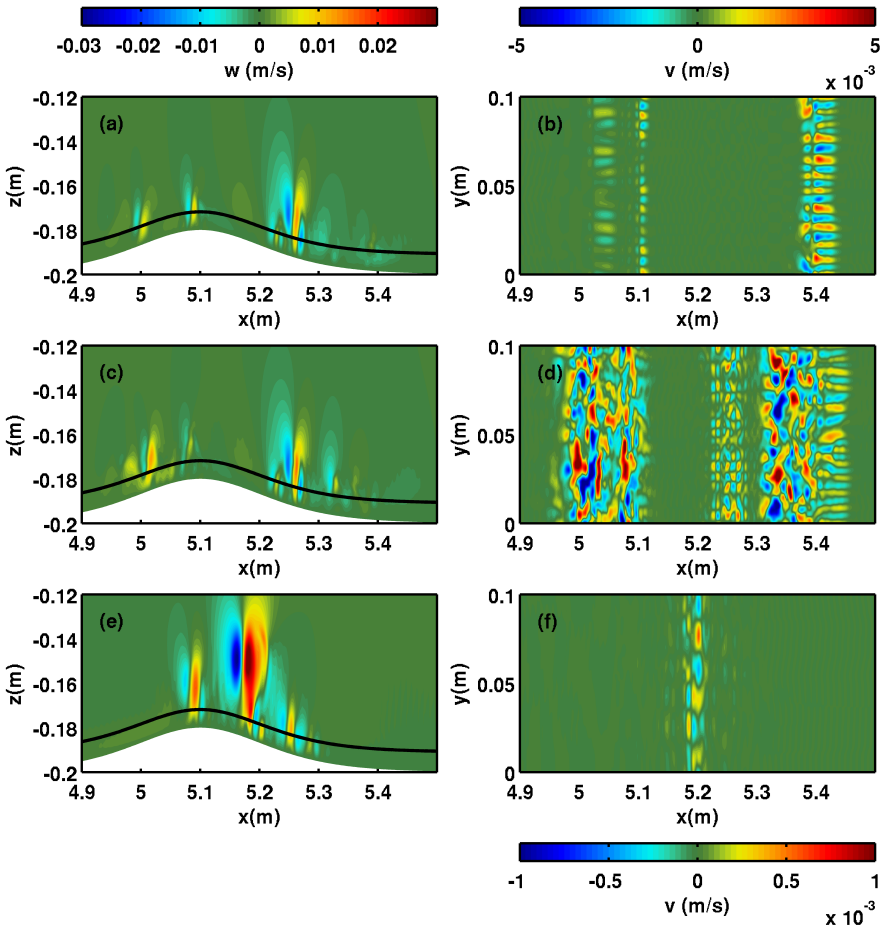

Figure 3.13: Comparing the vertical and spanwise velocities for the 3D simulations at $t = 40$ s. Panels (a), (c) and (e) are $x - z$ slices of the vertical velocity field for the small perturbation, large perturbation and dye simulations, respectively. The vertical velocity is saturated at 0.02 ms^{-1}. Panels (b), (d) and (f) are $x - y$ slices of the spanwise velocity along the black contours in (a), (c) and (e), respectively. The spanwise velocity is saturated at 0.005 ms^{-1} in (b) and (d), and at 0.001 ms^{-1} in (f). The black contours are all at the same level, approximately 0.01 m above the topography.

topography; investigation of this is left as a future research direction. Nevertheless, these vertical velocities coupled with the high extension of the vortices into the water column suggests that the unstratified case would be very efficient at cross-BBL transport.

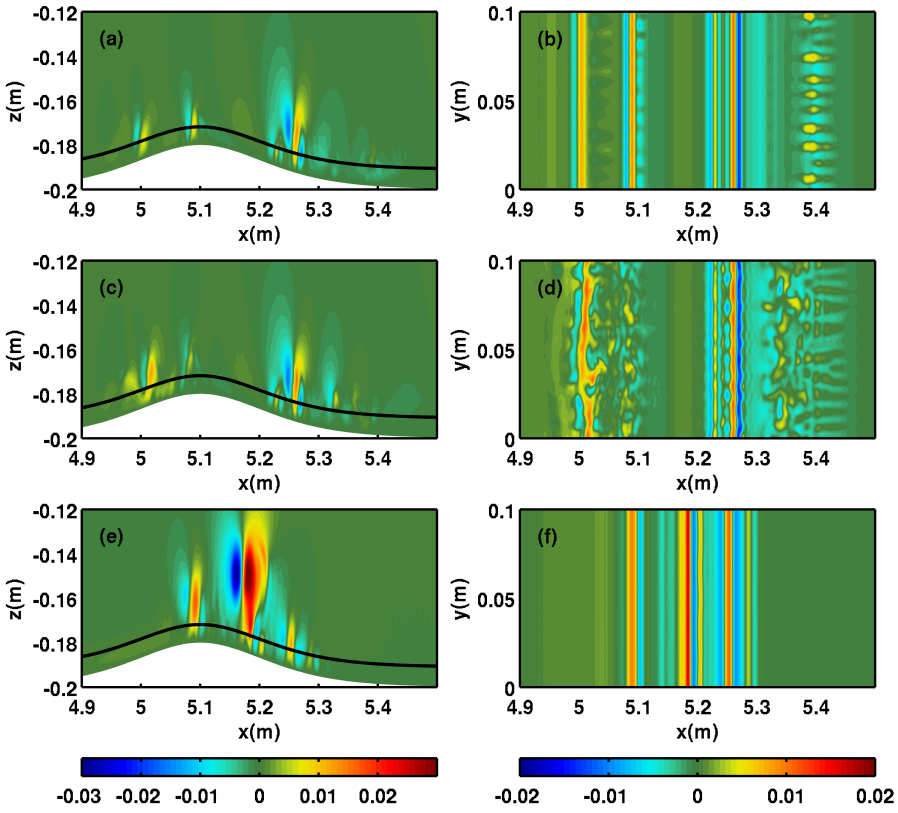

Figure 3.14: Comparison of the vertical velocities for the 3D simulations at $t = 40$ s. Panels (a), (c) and (e) are $x - z$ slices of w for the small perturbation, large perturbation and dye cases, respectively. These plots are saturated at 0.03 ms^{-1}. Panels (b), (d) and (f) are the corresponding $x - y$ slices of w along the black contours, and are saturated at 0.02 ms^{-1}. The black contours are identical to those in Figure 3.13.

Keep in mind that the nepheloid layer already contains suspended material which is much finer and lighter than the unsuspended bottom sediment, so that a high enough bed shear stress is not required for moving these suspended sediments higher into the water column. All that is needed are strong enough vertical velocities. Panels (a) and (c) of Figures 3.13 and 3.14 indicate that both bottom-stratified cases still have the potential to transport the lighter material in the nepheloid layer further up into the water column,

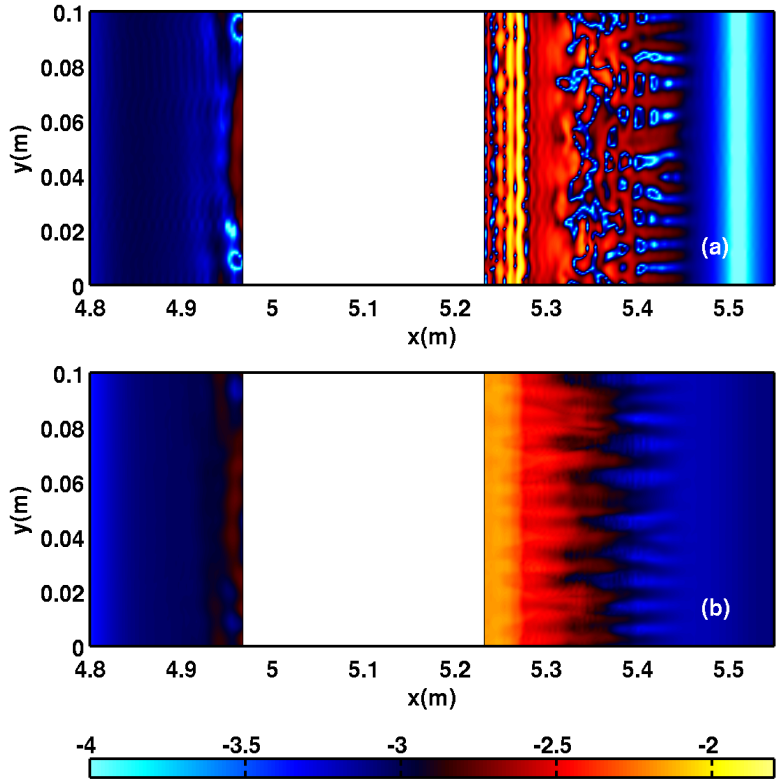

Figure 3.15: Net transport for a fixed height of $z = -0.19$ m. The base 10 logarithm of the absolute value of w is plotted. The hill is indicated by the white rectangular box. Panel (a) shows the logarithm of the net transport at time $t = 40$ s, whereas (b) shows the logarithm of the net transport averaged over $t = 36$ s to $t = 40$ s.

albeit only about 15% from the bottom. In the event that the vertical velocities are too weak for actual suspended particles to be lifted higher into the water column, there can still be chemical transport across the BBL and BNL.

Comparison of the right-hand panels of Figures 3.13 and 3.14 shows that there is very little 3D structure in the dye simulation, corroborating the observations made on the basis of the scaled spanwise standard deviation of kinetic energy plots. There is only a

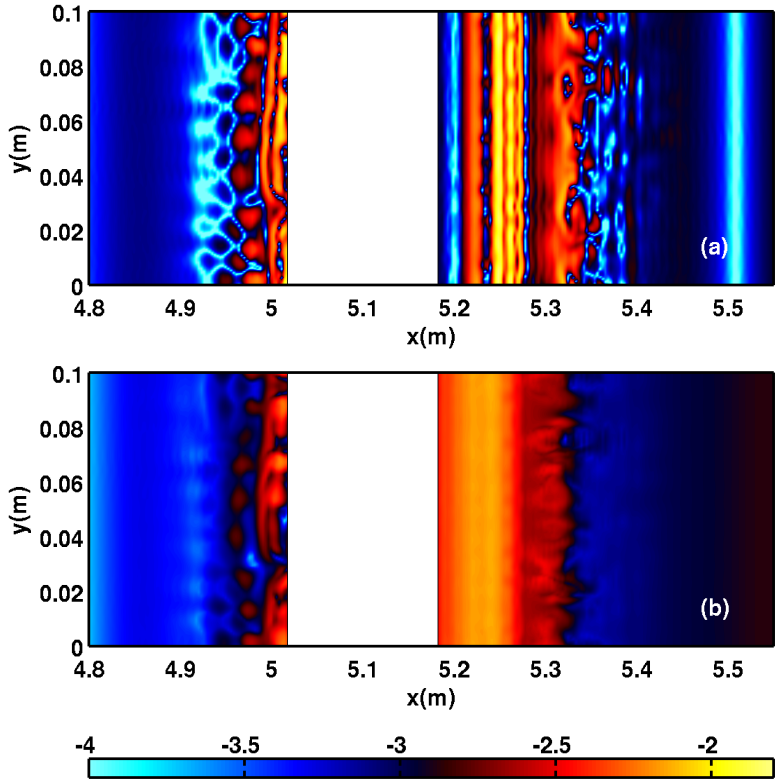

Figure 3.16: Net transport for a fixed height of $z = -0.185$ m. The base 10 logarithm of the absolute value of w is plotted. The hill is indicated by the white rectangular box. Panel (a) shows the logarithm of the net transport at time $t = 40$ s, whereas (b) shows the logarithm of the net transport averaged over $t = 36$ s to $t = 40$ s.

narrow region of spanwise velocities centred at about 5.2 m in panel (f) of Figure 3.13, and no visible 3D structure indicated by the vertical velocity field in panel (f) of Figure 3.14. Secondly, although the spanwise and vertical velocities for the small and large perturbation cases are comparable, there is a significantly larger region of 3D flow near the boundary for the large perturbation case. Panel (d) of Figure 3.13 makes this quite clear. Most of the 3D region contains spanwise velocity magnitudes in the range of 0.004 ms^{-1} to 0.005 ms^{-1} for the large noise case, compared to typical spanwise velocity magnitudes of 0.003 ms^{-1}

for the small noise case. It is also possible to deduce that in the case of an unstratified bottom, the areal extent of chemical cross-BBL transport would be less in comparison to having a nepheloid layer, since the region containing vertical velocities near the bottom boundary is less when compared to the large perturbation case at $t = 40$ s (panels (d) and (f) in Figure 3.14). Instability regions extend further out on the left side of the hill for the bottom-stratified simulations compared to the dye simulation.

The above results for the large noise, bottom-stratified simulation have shown that chemical cross-BBL transport and sediment pumping of finer and lighter materials can occur. The time average of the net transport at a fixed height is calculated to give an indication of where and how much sediment and chemical transport is most likely to occur. Since we are interested in transport both into and out of the near-bottom region, the absolute value of the vertical velocity is used as a measure for the net transport. Due to the mapped grid, the $w-$field is interpolated to a fixed height before further calculations are performed.

Figures 3.15 and 3.16 show the net transport for $z = -0.19$ m (the near-bottom pycnocline location) and $z = -0.185$ m respectively. The base 10 logarithm of the absolute value of w at $t = 40$ s is plotted in panels (a), whereas the base 10 logarithm of the time-averaged absolute value of w from $t = 36$ s to $t = 40$ s is plotted in panels (b). The hill is indicated by the white box. At $t = 40$ s there is more net transport on the right side of the hill for the two fixed heights because more of the instability region is located on the right side. The region of maximum net transport lies between $x = 5.25$ m and $x = 5.28$ m, which corresponds to the location of the largest vortices (see panel (c) of Figure 3.14). For these two heights, the maximum net transport based on panels (a) in Figures 3.15 and 3.16 is very close: 0.0155 ms^{-1} (or approximately -1.81 on the log scale) for $z = -0.19$ m, and 0.0157 ms^{-1} (or approximately -1.80 on the log scale) for $z = -0.185$ m. It should be noted that the vertical velocities due to the wave alone are no greater than 0.003 ms^{-1} in size for a fixed height of $z = -0.185$ m, and are therefore roughly a magnitude smaller than the maximum net transport, suggesting that the instabilities do indeed increase the likelihood of cross-BBL transport. Notice that $z = -0.185$ m captures more of the instabilities on the left side of the hill, which contains some of the higher net transport regions.

Panels (a) in both Figures 3.15 and 3.16 give little new information, if any, when compared to the $x - z$ slice shown in panels (c) and (d) of Figure 3.14. However, the time-averaged net transport can be useful for indicating whether a large enough net transport acts long enough for there to be systematic pumping of sediments. It can also show the areas where most of the cross-BBL transport will occur. The region containing the highest time-averaged net transport also occurs to the right of the hill in both panels (b). For the height $z = -0.185$ m, this region takes the shape of a band (yellow-orange in colour)

from $x = 5.19$ m to 5.26 m, and is larger than the yellow-orange band for $z = -0.19$ m in panel (b) of Figure 3.15. The typical velocities in the yellow-orange regions are in the $0.006 - 0.007$ ms^{-1} range. There are a small number of spots on the left side of the hill for $z = -0.185$ m where the time-averaged net transport is on the higher end. We can take a value of -2.5 on the logarithm scale, or approximately 0.0032 ms^{-1}, to define where the net transport is significant. Thus, the percentage of the topography in panel (b) of Figure 3.16 that has significant net transport is 16.5%, and the ratio of net transport on the left side of the hill to the right side is 0.06.

3.4 Internal Solitary Wave of Elevation

ISWs of elevation are less frequently observed in the field when compared to ISWs of depression. However, their interaction with topography is just as important when they are present in water bodies. For example, large-amplitude ISWs of elevation have been observed propagating shoreward on the Oregon shelf [32] and in the shallow waters near the Massachusetts coast (wave amplitude nearly one half the 25 m water depth)[56]. These waves have been observed to generate high bed shear stress on the sea floor, indicating their importance in sediment resuspension [32]. Furthermore, they can possess recirculating cores, which transport water upslope as they shoal so that the dense ocean water mixes with the homogeneous shelf water [32, 9].

This section presents the results of the various numerical simulations that were performed with the ISW of elevation: the last five cases given in Table 3.1. It takes the same format as the previous section on the ISW of depression where the 2D results comparing the bottom-stratified and dye runs are presented and discussed in the first section, followed by a discussion of the 3D results. As the wave passes over the hill, a novel gravity current due to the forcing of the wave currents is formed, which subsequently becomes unstable with mixing in the current front. The region of intense mixing moves along with the wave for some distance before being dissipated. Potential implications for sediment transport are also addressed.

3.4.1 Two-Dimensional Simulations

Similar to the previous section on the ISW of depression, the general features of an ISW of elevation will first be highlighted before addressing any results. The density, horizontal and vertical velocity fields for the ISW of elevation used in this work are shown in Figure 3.17.

Panel (a) shows that the portion of the nepheloid layer that is directly beneath the wave takes on the shape of a wave crest as the wave moves along the domain.

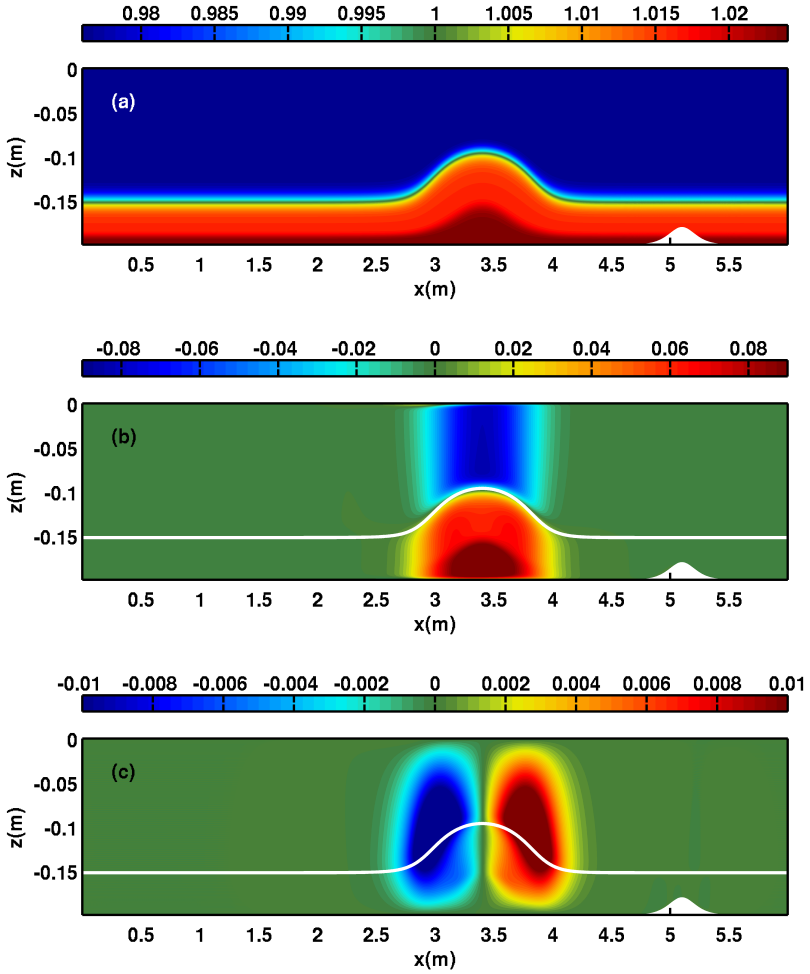

Figure 3.17: ISW of elevation with near-bottom stratification. The wave and its currents are shown for time $t = 3$ s before the wave reaches the hill. The entire computational domain is shown. (a) Density plot saturated between 0.976 kg/L and 1.024 kg/L. The pycnocline of the near-bottom stratification lies below the hill crest. (b) Horizontal velocity saturated at 0.09 ms^{-1}. (c) Vertical velocity saturated at 0.01 ms^{-1}. The white density contours in panels (b) and (c) correspond to a density of 1 kg/L.

The horizontal and vertical wave-induced currents for an ISW of elevation are opposite

to those in an ISW of depression. The horizontal wave currents are leftward above the wave crest and rightward below, as seen in panel (b). Recall that this particular wave is propagating from the left to the right, since the direction of wave propagation determines the orientation of the wave-induced currents. There are two interesting differences to notice between ISWs of elevation and depression. Firstly, the jet that trails behind an ISW of elevation is extremely weak when compared with the wave itself. In fact, for the present wave, the jet is indiscernible for the colour saturation used. The second difference to observe is that the positive (rightward) horizontal currents are strongest in the bottom, centre region of the wave. Finally, one can see from panel (c) that the vertical wave-induced currents are upward (positive) in the front section of the wave, and are downward (negative) in the rear section.

Figure 3.18 shows an overview of what transpires in the 2D simulation as the ISW of elevation passes over the hill. The wave is initialized on the left end of the domain and propagates to the right. Panel (a) shows the entire computational domain before the wave arrives at the hill. The crest of the near-bottom stratification directly below the wave extends about 0.02 m higher into the water column than the topographic hill does. As the wave approaches the hill at $t = 13$ s, the wave pycnocline is nearly unchanged, but the near-bottom crest of dense fluid undergoes shoaling because of direct contact with the hill. Since the near-bottom pycnocline is initially lower than the hill crest, there is a horizontal gap in the fluid density on the right side of the hill at the time when the denser fluid on the left shoals and moves up to the hill crest. This is a precursor for the formation of a gravity current, as there are now two distinct regions of dense fluid in the near-bottom region [59]. The density difference is approximately 0.8%.

As the wave continues to move over the hill, there are disturbances in the wave pycnocline as shown in panel (c) at $t = 16$ s. The near-bottom fluid has now crept over from the left side of the hill, resulting in the beginning stages of a gravity current formation. The front edge of the dense, near-bottom fluid is curled upward, a characteristic feature of the head of a gravity current. A comparison with the dye field for the unstratified bottom case is presented in Figure 3.19. From examination of panels (a) and (c), we see that the curling corresponds to the vertical shear region at $x = 5.4$ m. This is absent in the dye simulation, illustrating that the density difference is indeed responsible. Panel (d) indicates that the vertical velocity for the dye case at the corresponding position is roughly half the size. The horizontal difference in density on the right side of the hill combined with the heavier region of fluid moving into the lighter fluid produces the gravity current [59], as seen at $t = 19$ s in panel (d) of Figure 3.18. Note that this is not a pure gravity current because there are significant horizontal velocities due to the wave in this region. It is also a short-lived gravity current, as the head of incoming denser fluid meets the denser fluid

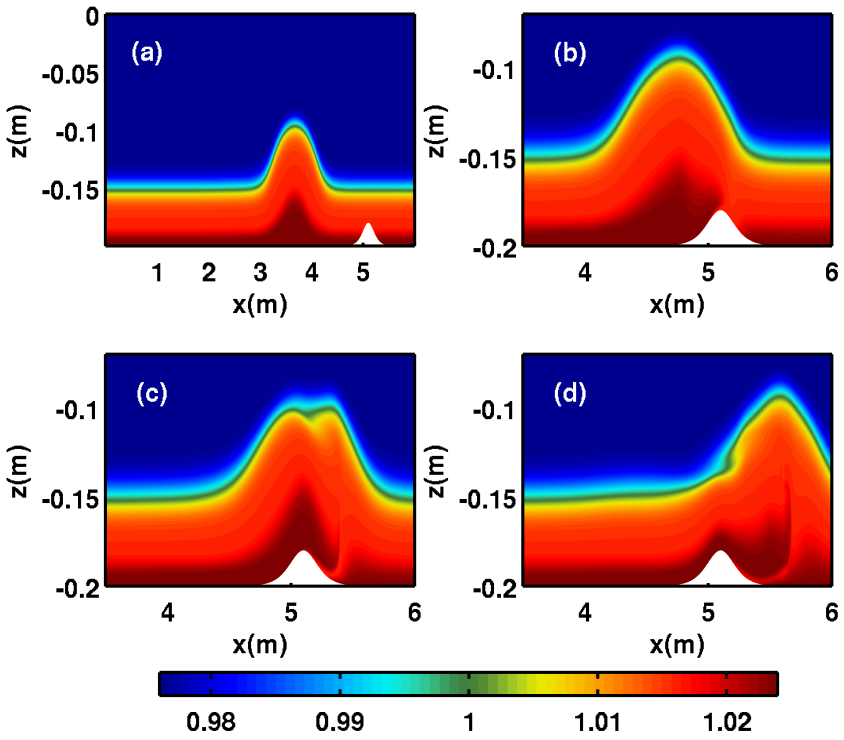

Figure 3.18: Density plots of the ISW of elevation as it propagates over the hill for the 2D simulation. (a) The wave before it reaches the hill at $t = 5$ s. The entire computational domain is shown. Panels (b), (c) and (d) focus on the right half of the domain as the wave interacts with the hill at times $t = 13$ s, $t = 16$ s and $t = 19$ s, respectively. The density is saturated between 0.976 kg/L and 1.024 kg/L.

a

on the right at about $t = 22$ s. Nevertheless, we shall maintain use of the term 'gravity current' for simplicity and lack of better terminology. The horizontal velocity field shows that the heavier fluid moves faster than the lighter fluid, which is also consistent for the early times in the instability evolution; see panel (a) of Figure 3.20.

Plots of the velocity fields at the time of the developed gravity current in panel (d) of Figure 3.18 is shown in Figure 3.20. At time $t = 19$ s, the wave crest is located at

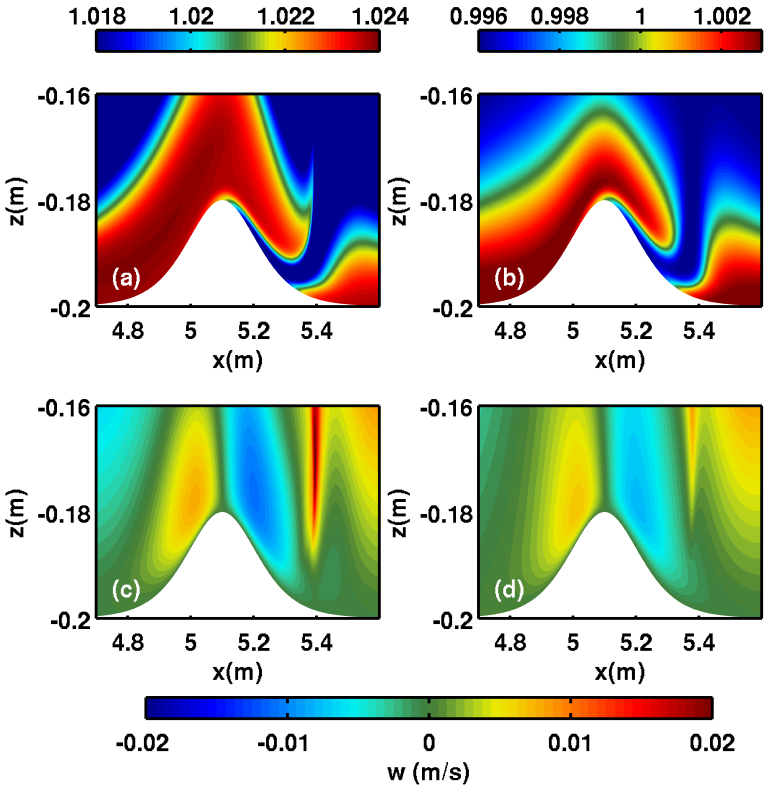

Figure 3.19: Comparison of some of the near-bottom dynamics between the bottom-stratified and dye case for $t = 16$ s. Panels (a) and (c) are density and vertical velocity plots for the bottom-stratified case, respectively. Panels (b) and (d) are dye and vertical velocity plots for the dye case, respectively. The vertical velocity is saturated at 0.02 ms^{-1}.

approximately $x = 5.6$ m. Panel (a) of Figure 3.20 shows the horizontal velocity field saturated at 0.1 ms^{-1}: it can be seen that these horizontal wave currents are positive and are strongest below the centre of the wave. At this time, the region of strongest horizontal currents (darkest red region) coinciding with the gravity current in panel (c), takes the shape and size of the gravity current. Comparison with the dye case in Figure 3.21 reveals that this feature is absent in an unstratified near-bottom region. The vertical velocity component saturated at 0.01 ms^{-1} is shown in panel (b) of Figure 3.20, and is approximately an order of magnitude smaller than the typical horizontal wave-induced current. We see that the vertical shear region at $x = 5.65$ m coincides with the leading edge of the gravity current where there is upward curling, as previously stated.

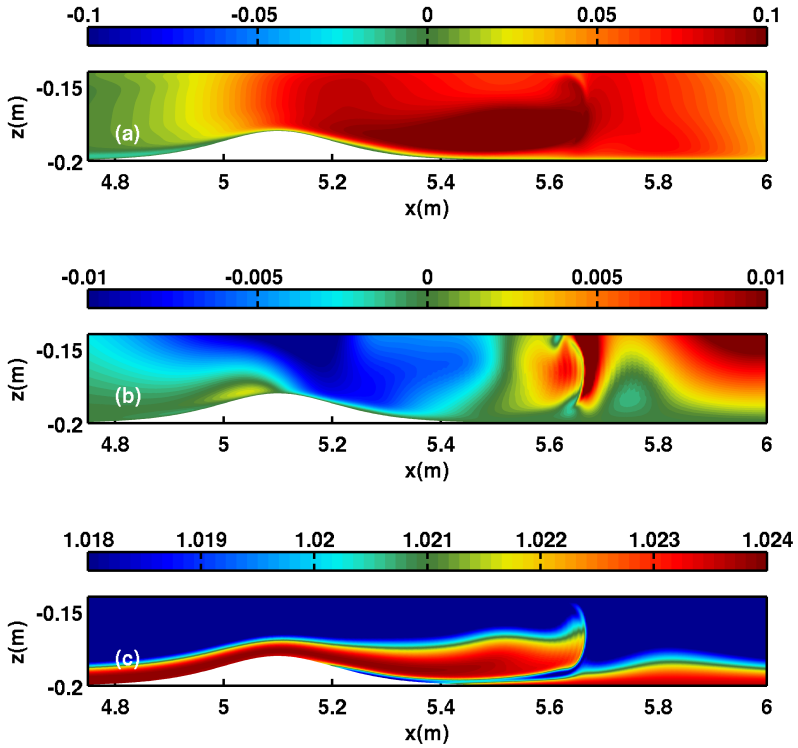

Figure 3.20: A more detailed look at the dynamics of the gravity current for the 2D case at time $t = 19$ s. The sub-section of the domain containing the gravity current is shown. (a) Horizontal component of velocity saturated at 0.1 ms^{-1}. (b) Vertical component of velocity saturated at 0.01 ms^{-1}. (c) Density saturated between 1.018 kg/L and 1.024 kg/L. The near-bottom stratification takes the form of a gravity current.

Thus, the 2D simulations for this particular model set-up reveal that the most significant difference between a stratified near-bottom region versus an unstratified near-bottom region is the formation of a novel type of gravity current that forms as the wave currents move the dense fluid on the left side of the hill over to the right. The presence of the gravity current alters the velocity fields in the near-bottom region (Figures 3.19 and 3.21). For the times shown above, there does not seem to be any indication of instabilities in the near-bottom region. However, a plot of the density field at $t = 27$ s shown in panel (b) of Figure 3.22 does reveal significant instabilities in what was the front region of the gravity current.

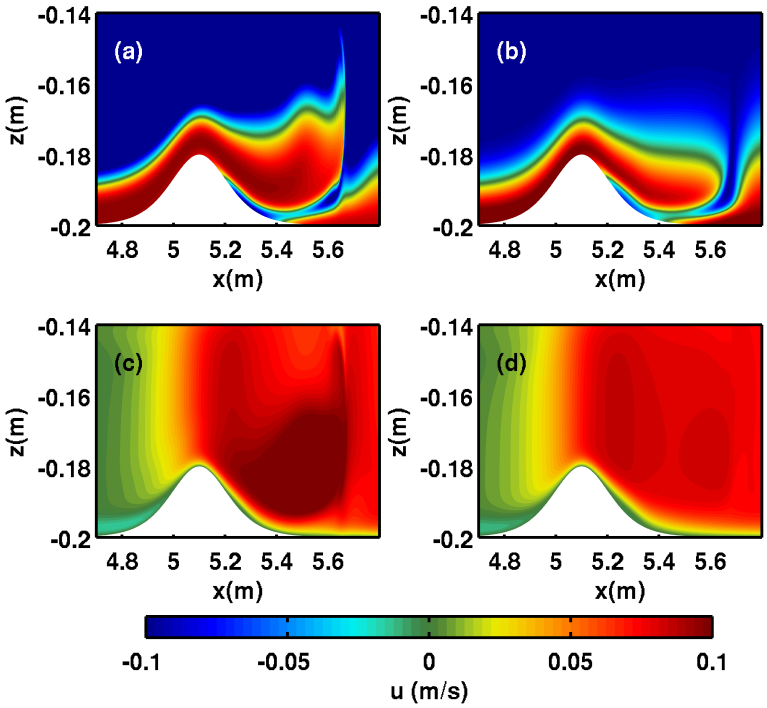

Figure 3.21: Contrasting the gravity current with the dye case at $t = 19$ s. Panels (a) and (c) are density and horizontal velocity plots for the bottom-stratified case, respectively. Panels (b) and (d) are dye and horizontal velocity plots for the dye case, respectively. The horizontal velocity is saturated at 0.1 ms^{-1}.

At the time of the onset of the instability, this region is no longer a gravity current and the resulting instability is essentially a variant of the Rayleigh-Taylor (R-T) instability. Nevertheless, this particular region moves along with the wave for some distance (at least 2 m from the hill crest) in both the 2D and 3D simulations, thus providing a mechanism for transporting fluid from above the nepheloid layer to regions where it can mix with the nepheloid layer. The 2D simulation at $t = 40$ s indicates that the energy in this region has dissipated, and there are now only some small disturbances in the near-bottom stratification. Due to computational run time, the 3D simulations were not run beyond $t = 32$ s. At $t = 32$ s the leading edge region (in the 3D large noise case) is still present, although both its size and the degree of mixing are reduced.

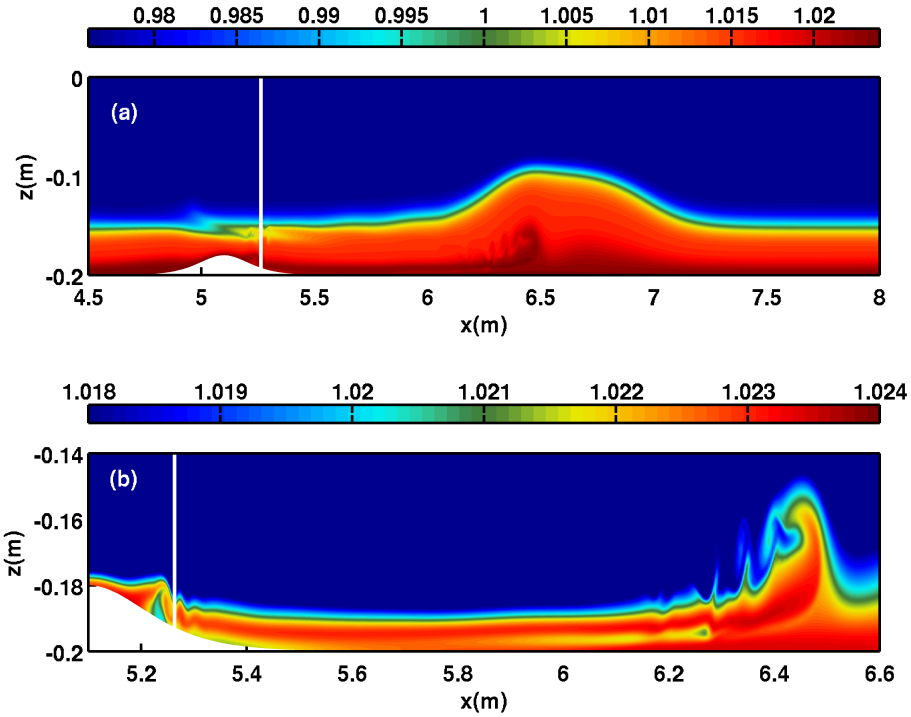

Figure 3.22: Density plots for the bottom-stratified simulation at $t = 27$ s. The periodic domain in the $x-$direction allows for the domain to be extended. Panel (a) shows the entire wave after it has fully cleared the hill. Panel (b) zooms in on the instabilities in the nepheloid layer. The vertical white line is used as an indicator to give an idea of where the BBL instability occurs.

The reader can also see from panel (b) in Figure 3.22 that there is some weak BBL separation that occurs on the right slope of the hill, after the wave has cleared the hill (the separation actually starts from about $t = 25$ s). Since light fluid is trapped under heavy fluid, a R-T instability develops, but it is not very energetic and dissipates quickly. In the dye case there is also BBL separation present which later results in vortex production. However, this is a result of secondary importance for the bottom-stratified case, since these instabilities are small and not as violent in comparison to the gravity current becoming unstable. Panel (b) of Figure 3.22 shows the marked difference in the size. This thesis therefore focuses on the gravity current and the corresponding instability.

3.4.2 Three-Dimensional Simulations

As was done for the ISW of depression, the effect of the noise amplitude will be investigated for the ISW of elevation propagating over a hill with a near-bottom stratification. The 2D simulations (Figure 3.18) showed that the generated instabilities are event-based: the passage of the wave over the hill triggers the instabilities. Two 3D runs involving the near-bottom stratification were performed. The perturbation magnitudes also differed by two orders of magnitude as with the wave of depression, where the larger one was chosen to be 1% of the absolute value of the maximum velocity in the 2D run at the time when the 3D run was initialized. The perturbation magnitudes were 1.1×10^{-3} ms^{-1} and 1.1×10^{-5} ms^{-1} for the large and small noise cases respectively. The dye simulation was also extended into the third dimension and used the conventional perturbation magnitude as in the large noise run (1.1×10^{-3} ms^{-1}). The three simulations were initialized at time $t = 14$ s, when the ISW begins interacting with the hill. See panel (b) of Figure 3.18 for an idea of where the wave is at $t = 14$ s. The data for the 3D simulations was saved every 0.25 seconds.

The 3D simulations have indicated that the gravity current head becomes unstable at an earlier time compared to the 2D simulations. Figure 3.23 illustrates what happens for the small and large noise cases after the wave crest has just passed the hill. The left panels correspond to the small noise simulation, and the right panels correspond to the large noise simulation. At time $t = 18.75$ s, panel (a) shows that the heavier fluid in the gravity current sits on top of a thin layer of lighter fluid for the small noise case. However, at this time for the large noise simulation, the lighter fluid trapped below the gravity current takes the form of two 'finger-like' structures, with the one on the right being almost 90° to the horizontal. These fingers are formed because of a Rayleigh-Taylor instability with an Atwood number of approximately 0.0022. The reader should note that in the present context, "finger" refers to the shape and there is no suggestion that the dynamical structures are related to salt fingers.

As time progresses, the R-T instability evolves and breaks down the front region of the gravity current in the large noise simulation. There is also considerable mixing of the fluid in the nepheloid layer. This is also the case for the small noise simulation, except that the R-T instability and subsequent break down is less energetic at the corresponding times. Observe that for both perturbation cases, the majority of the instability grows in the leading edge region of the gravity current, as is commonly observed in the laboratory and in simulations [59, 26, 25]. A spanwise ($y-$direction) average of the density fields is given in Figure 3.24, which takes an identical format to Figure 3.23. We can notice that the small perturbation case is still very 2D even at $t = 20$ s, as the layer of trapped, light fluid in panel (c) is almost the same shape as the trapped layer in panel (c) of Figure 3.23.

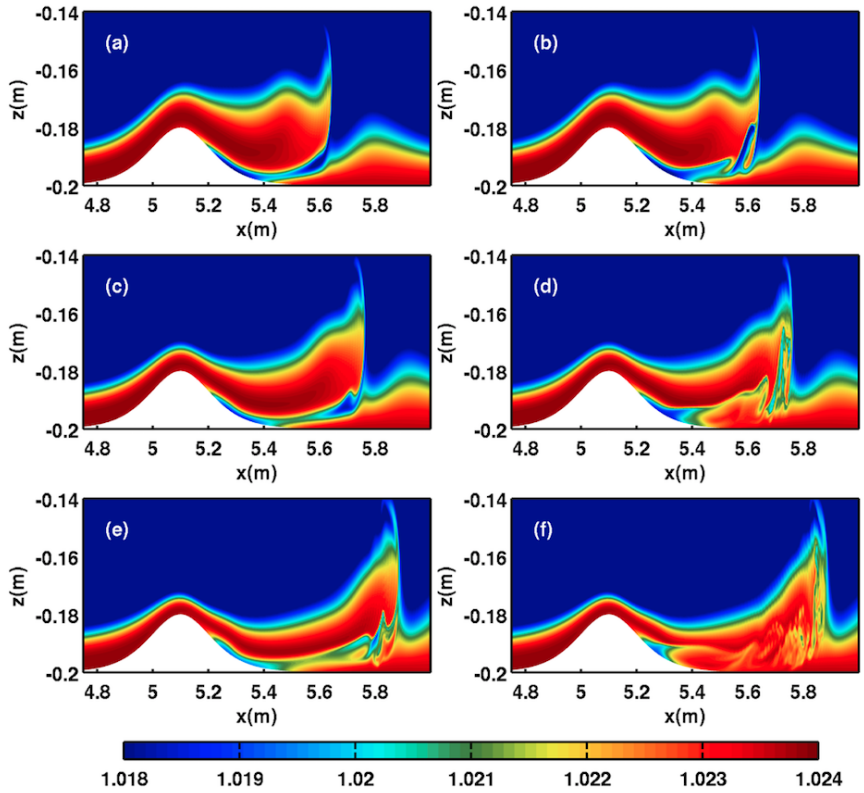

Figure 3.23: Differences in the evolution of the instability for the small and large perturbation runs as seen through an $x - z$ slice of the density fields. Panels (a), (c) and (e) are density plots of the small perturbation run at times $t = 18.75$ s, $t = 20$ s and $t = 21.25$ s, respectively. Panels (b), (d) and (f) are density plots of the large perturbation run at times $t = 18.75$ s, $t = 20$ s and $t = 21.25$ s, respectively. Density plots are saturated between 1.018 kg/L and 1.024 kg/L.

Three-dimensionalization is much more apparent at $t = 21.25$ s when the two (e) panels are compared. The finger-like structures at $t = 18.75$ s have been smeared out in the spanwise average for the large perturbation case, which can indicate a reasonable amount of three-dimensionalization already present at this time. Further details of the degree of three-dimensionalization for both cases will be addressed when discussing the scaled spanwise standard deviation of kinetic energy. Additionally, we can confirm a previous statement based on Figure 3.23 about the majority of mixing occurring in the front of the gravity current in both cases. The mixing region at the front extends higher (approximately

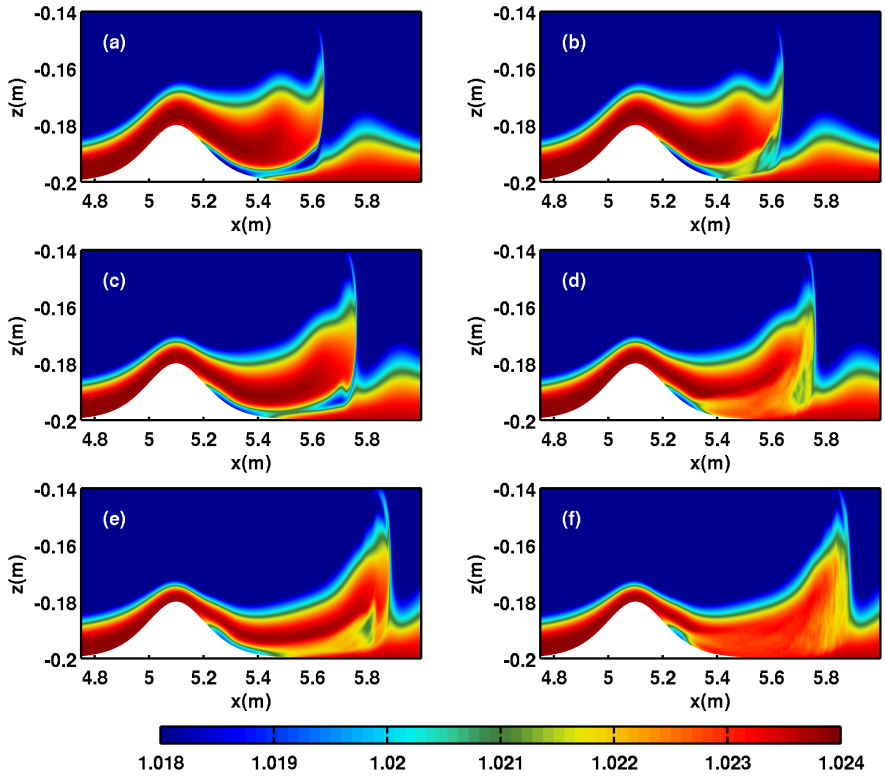

Figure 3.24: Differences in the evolution of the instability for the small and large perturbation runs as seen through the spanwise average of the density fields. Panels (a), (c) and (e) are density plots of the small perturbation run at times $t = 18.75$ s, $t = 20$ s and $t = 21.25$ s, respectively. Panels (b), (d) and (f) are density plots of the large perturbation run at times $t = 18.75$ s, $t = 20$ s and $t = 21.25$ s, respectively. Density plots are saturated between 1.018 kg/L and 1.024 kg/L.

0.01 m) from the bottom for the large noise case, indicating that there is likely to be more cross-BBL transport when compared to the small noise case.

However, there is an absence of Kelvin-Helmholtz instabilities and billow formation in the top of the gravity current. Nevertheless, lobe-cleft instabilities are generated for both the large and small perturbation cases. Figure 3.25 illustrates the lobe-cleft pattern that arises in the gravity current front for the large perturbation case at $t = 20$ s, while Figure 3.26 illustrates the lobe-cleft pattern for the small perturbation case at $t = 21.25$ s.

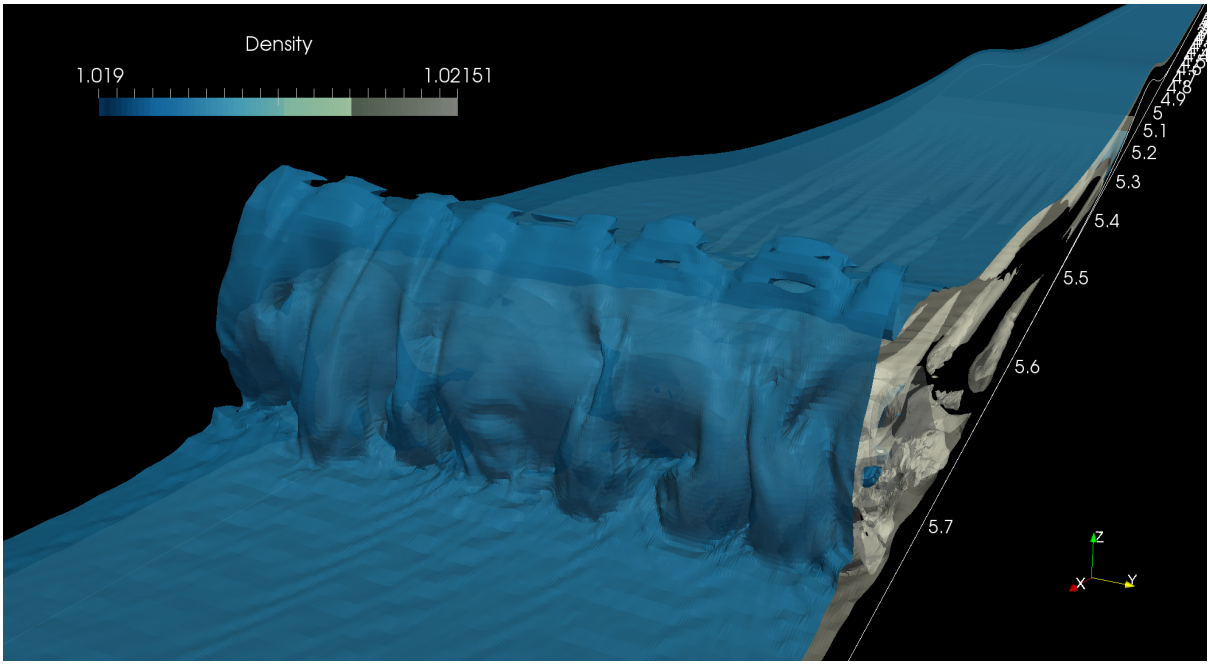

Figure 3.25: A 3D visualization of the lobe-cleft instability for the large noise, bottom-stratified simulation at $t = 20$ s. The blue isosurface is at a density value of 1.0195 and the grey isosurface corresponds to a density of 1.0215.

It is important to mention that the dye simulation does not exhibit any significant three-dimensionalization for the times discussed above, with the maximum scaled spanwise deviation of kinetic energy from $t = 20$ s to $t = 22$ s being in the vicinity of 1.5×10^{-4}. There is no visible qualitative difference from the 2D dye simulation, and so the detailed results of this particular simulation will not be presented. Figures 3.27 and 3.28 show evolution plots of the scaled spanwise standard deviation of kinetic energy for the small and large perturbation cases respectively. For the small perturbation case, two things can be observed. The first is that the instability region grows in time; secondly, the scaled standard deviation of kinetic energy increases by almost two orders of magnitude from $t = 18.75$ s to $t = 21.25$ s. At time $t = 21.25$ s, the scaled spanwise deviation of kinetic energy averages about 0.15 to 0.2 in the instability region, indicating that three-dimensionalization is important. However, for the large perturbation case, the degree of three-dimesionalization at $t = 18.75$ s is already significant (the values are between 0.15 and 0.2). The instability region also grows with time for the large noise simulation, but the maximum scaled spanwise deviation of kinetic energy remains approximately constant,

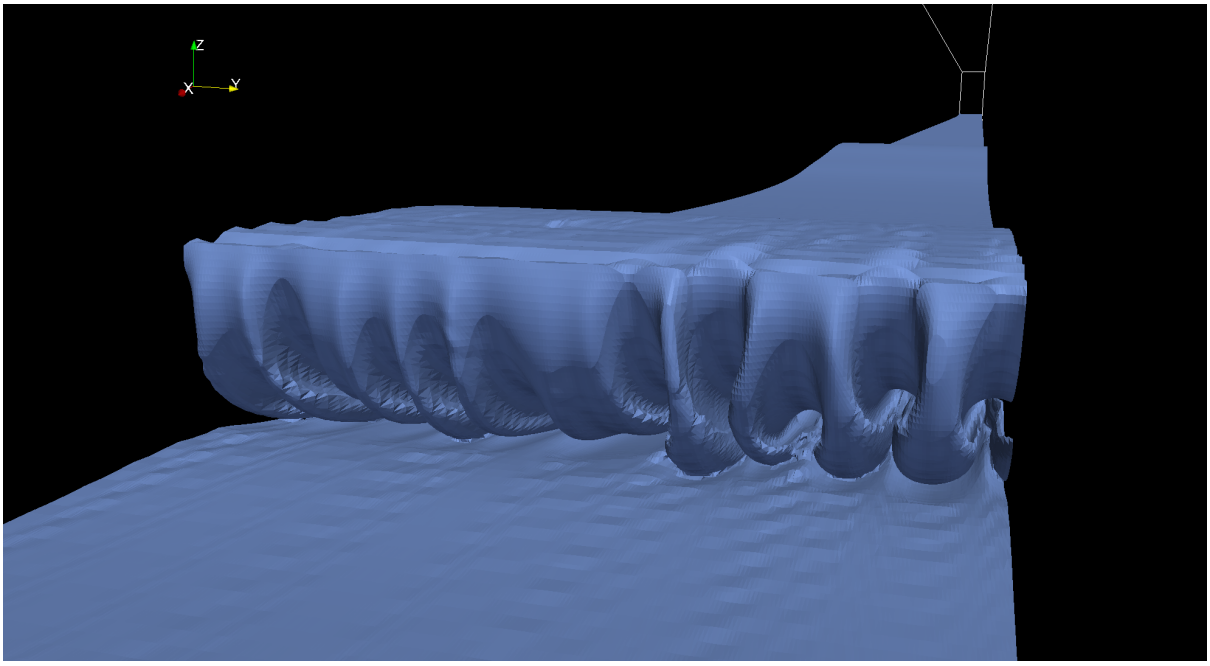

Figure 3.26: A 3D visualization of the lobe-cleft instability for the small noise, bottom-stratified simulation at $t = 21.25$ s. The blue isosurface is at a density value of 1.022.

indicating that most of the three-dimensionalization has already set in at an earlier time. The region containing the higher values (0.15 to 0.22) decreases from $t = 20$ s to $t = 21.25$ s for the large noise simulation. These two plots also reinforce the observation from Figures 3.23 and 3.24 that the instability region for the large perturbation case is more energetic and spans a greater area, allowing for more mixing and cross-BBL transport.

The 3D structure in terms of the spanwise velocity for the small perturbation run is presented in Figure 3.29 for time $t = 21.25$ s. This figure shows the 3D structure at different heights of the instability region, indicated by the white contours in panel (a). It should be noted that these contours are not parallel to the horizontal because of the use of a mapped grid, which is a consequence of having bottom topography. Apart from the adjoining red and blue dots in panel (b) at $x = 5.83$ m, there is negligible 3D structure at this vertical location of the instability. The two dots correspond to a region above the little crest of lighter (blue/green) fluid in panel (a).

Amongst the three $x-y$ slices shown in Figure 3.29, the greatest amount of 3D structure is seen in panel (c), which corresponds to a height of about 0.01 m from the bottom. This is not very surprising as this contour passes through a large portion of the entrapped region

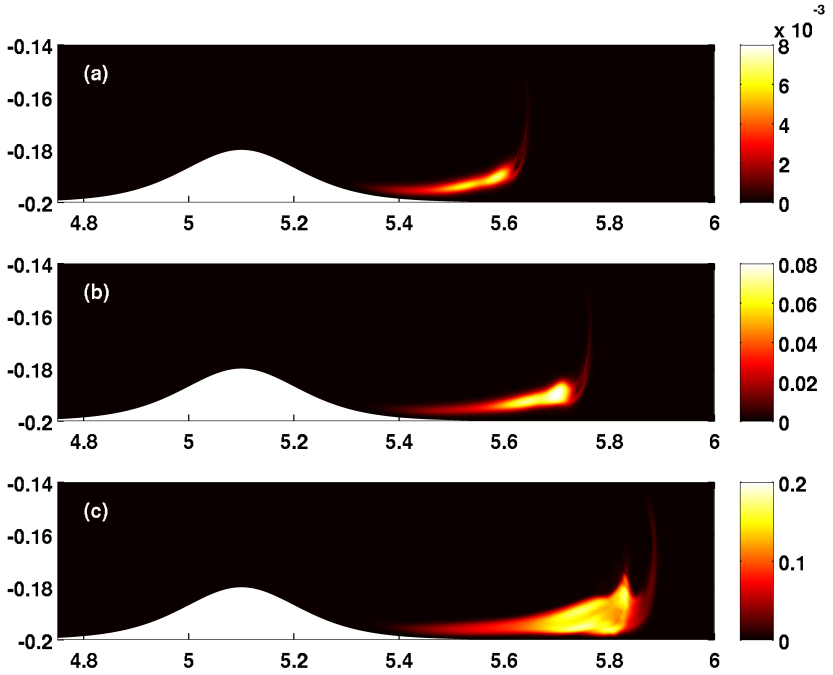

Figure 3.27: Plots of the spanwise standard deviation of kinetic energy scaled by the maximum kinetic energy for the small perturbation simulation at three different times. (a) $t = 18.75$ s, (b) $t = 20$ s, (c) $t = 21.25$ s.

of lighter fluid. Interestingly, this corresponds to the depth at which the near-bottom pycnocline is centred. The bulk of this 3D structure spans a horizontal distance of about 0.1 m. Nearer the bottom of the domain, the red/blue patches shown in panel (d) are smaller and span a shorter horizontal distance than those in panel (c). The spanwise velocity magnitudes in the red/blue patches of (c) and (d) are comparable, the maximum being around 0.01 ms^{-1}.

The effect of the perturbation amplitude on the three-dimensionalization is quite apparent in Figure 3.30. This figure compares $x-y$ slices of the spanwise and vertical velocity fields in the instability region for the small and large perturbation cases at time $t = 20$ s. The 3D structure for both spanwise and vertical velocity fields at this level of the instability region is well developed for the large noise case, spanning about twice the area as that of the small noise case. The velocity magnitudes for the large noise case are, on average, about twice as large as those in the small noise case, with most of the velocities

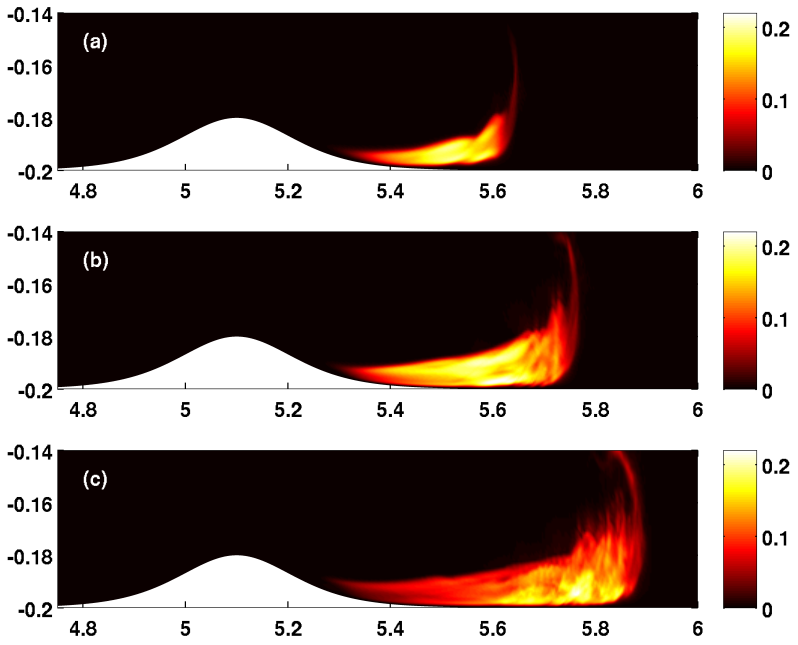

Figure 3.28: Plots of the spanwise standard deviation of kinetic energy scaled by the maximum kinetic energy for the large perturbation simulation at three different times. (a) $t = 18.75$ s, (b) $t = 20$ s, (c) $t = 21.25$ s. All three colourbars are saturated at 0.22.

reaching full colour saturation in the large noise simulation. It is worth mentioning that for the small noise case, the vertical velocities in the instability region are roughly twice as large as the corresponding spanwise velocities. Figure 3.30 clearly implies that there is a greater potential for cross-BBL transport in the large noise case, as well as mixing of the fluid in the nepheloid layer with some of the overlying fluid in a larger geographical area at this time.

Figure 3.31 compares the 3D structure for the small perturbation case at two times. It takes the same format as Figure 3.30, except that the bottom two panels are now replaced by the small perturbation run at a later time ($t = 21.25$ s.) The red and blue patches have grown and developed into structures that now span about twice as much area, and with stronger spanwise and vertical velocities. At this time, the majority of vertical velocities in the instability region are at full colour saturation (0.01 ms^{-1}), similar to the large perturbation case at $t = 20$ s in Figure 3.30. Notice that the instability region has shifted

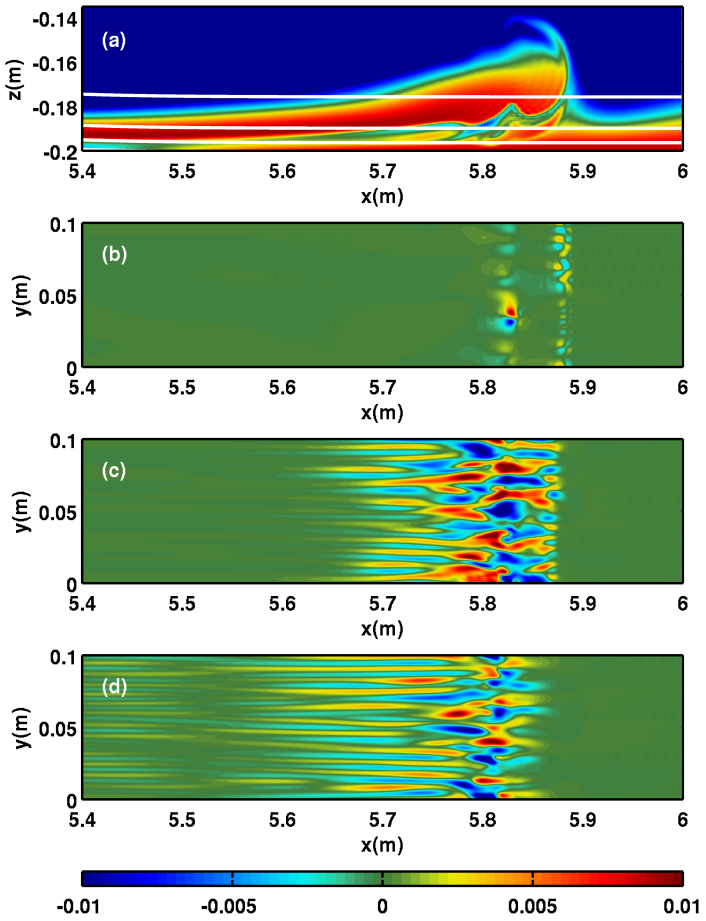

Figure 3.29: Three-dimensional structure for the small perturbation simulation at different $x-y$ slices for time $t = 21.25$ s. Panel (a) shows an $x-z$ slice of the density field with three white contours indicating where the $x-y$ slices are taken. The contours from top to bottom correspond to heights of approximately $z = -0.176$ m, $z = -0.190$ m, and $z = -0.196$ m respectively. (b) Spanwise velocity component corresponding to the top contour. (c) Spanwise velocity component corresponding to the middle contour. (d) Spanwise velocity component corresponding to the bottom contour. The spanwise velocity is saturated at 0.01 ms^{-1}.

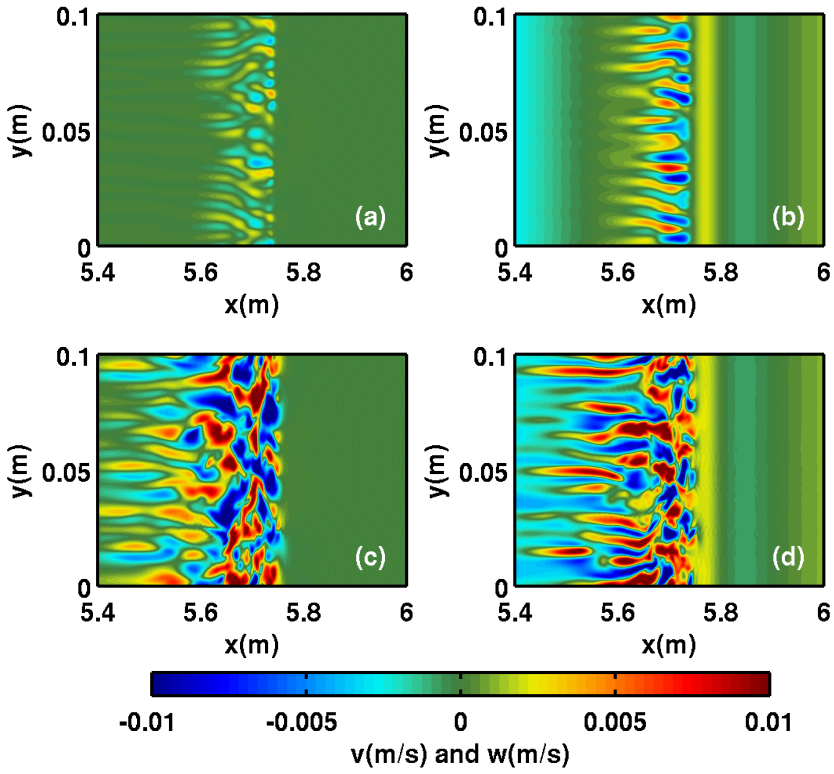

Figure 3.30: Comparison of the 3D structure between the small and large perturbation simulations for the near bottom region at time $t = 20$ s. The $x - y$ slices are taken at a height of approximately $z = -0.191$ m. Panels (a) and (b) are the spanwise and vertical velocity components, respectively, for the small perturbation simulation. Panels (c) and (d) are the spanwise and vertical velocity components, respectively, for the large perturbation simulation. Both the spanwise and vertical velocity components have been saturated at 0.01 ms^{-1}.

to the right, since this region moves along with the wave, as previously mentioned. It is interesting to observe that even at this later time, the areal extent of the 3D structure (and to a degree, the amount of three-dimensionalization) is still less than that of the large perturbation case at $t = 20$ s (see panels (c) and (d) of 3.30). This can be seen by revisiting the scaled spanwise standard deviation of kinetic energy plots. Although the values of the scaled spanwise standard deviation of kinetic energy are close for the large noise case at

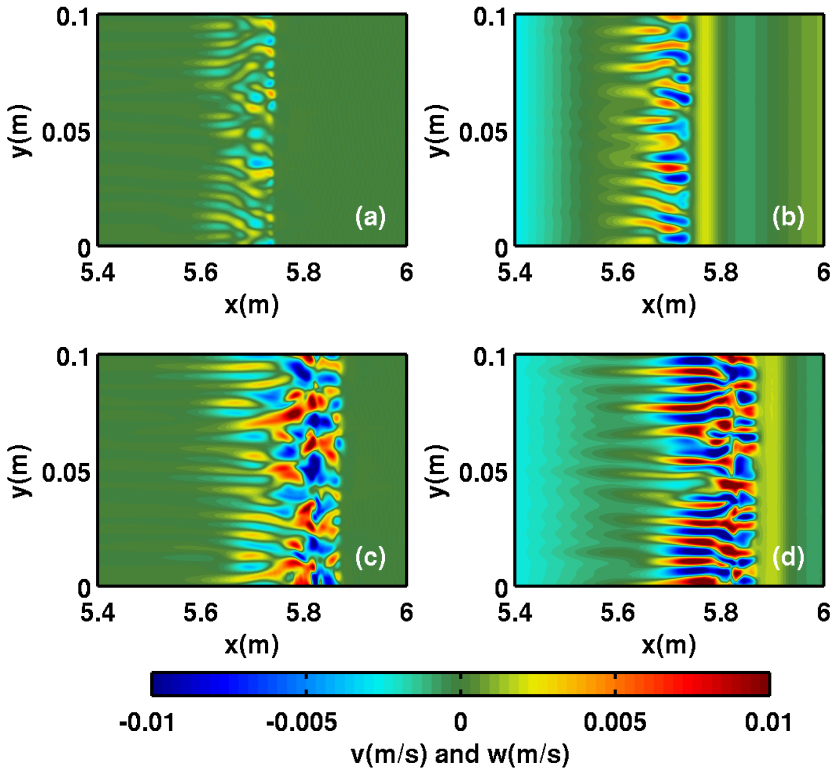

Figure 3.31: Three-dimensional structure for the small perturbation simulation at two different times near the bottom region. The $x-y$ slices are taken at a height of approximately $z = -0.191$ m. Panels (a) and (c) are spanwise velocity plots at times $t = 20$ s and $t = 21.25$ s, respectively. Panels (b) and (d) are vertical velocity plots at times $t = 20$ s and $t = 21.25$ s, respectively. Both the spanwise and vertical velocity components have been saturated at 0.01 ms^{-1}.

$t = 20$ s and the small noise at $t = 21.15$ s, the instability region for the small noise case is smaller and has shifted to the right of the domain, i.e. the three-dimensionalization sets in later. Nevertheless, comparison of Figures 3.30 and 3.31 suggests that the small perturbation case has a similar potential for cross-BBL transport and mixing of fluid in the nepheloid layer as the large perturbation case does, albeit over a smaller geographical region.

The final set of figures to conclude this comparison shows density isosurfaces in the instability region. Figures 3.32 and 3.33 take the same format and show density isosurfaces at different levels in the instability. Although Figure 3.32 shows the small perturbation case at a later time than the large perturbation case, one can extract two of the conclusions made above by comparing these two figures: (1) the large perturbation case has a greater degree of three-dimensionalization, and (2) the region of 3D structure is larger for the large perturbation case.

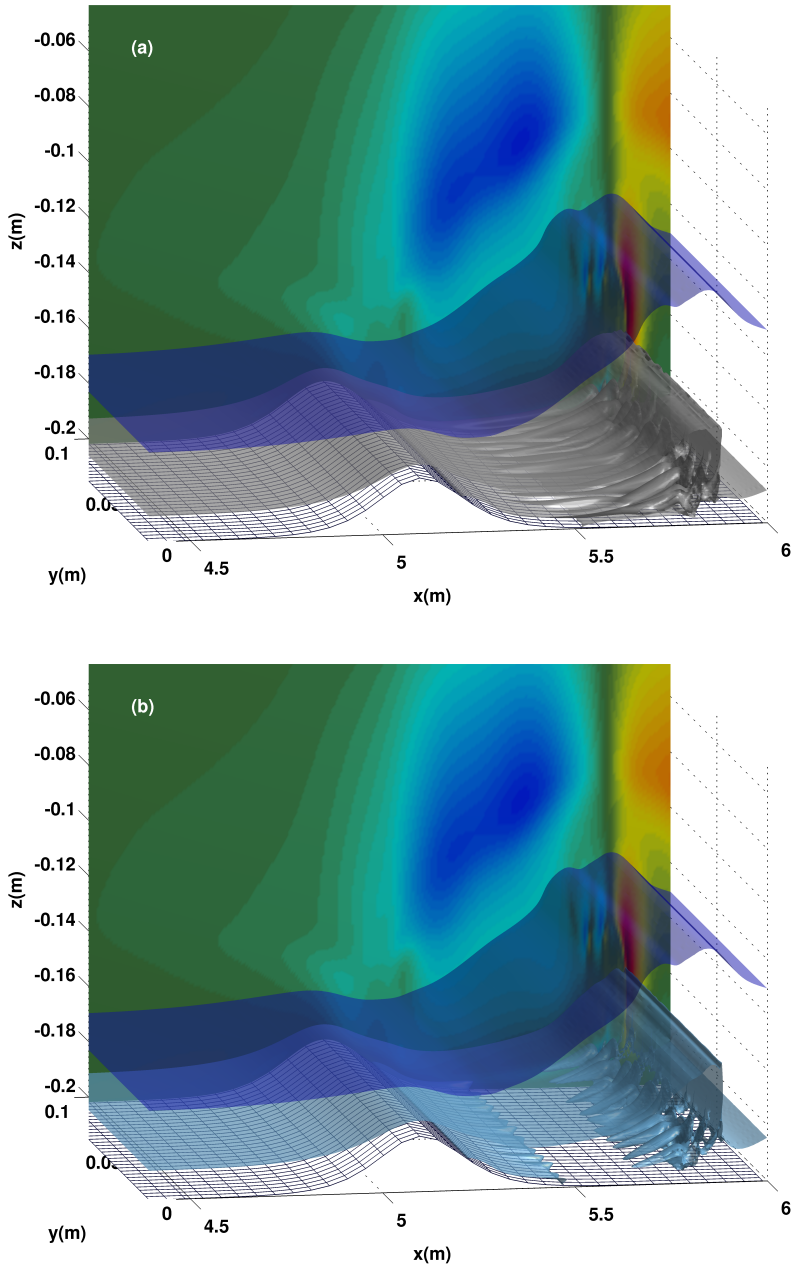

Figure 3.32: Density isosurface plots for the small perturbation run at time $t = 21.25$ s. The top indigo isosurface corresponds to a density value of 1.015 kg/L and the background is an $x - z$ slice of the vertical velocity. The location of the wave can be seen by the wave-induced currents (the large blue and yellow-orange regions in the background). (a) The grey isosurface corresponds to a density value of 1.022 kg/L, (b) The light blue isosurface corresponds to a density value of 1.021 kg/L.

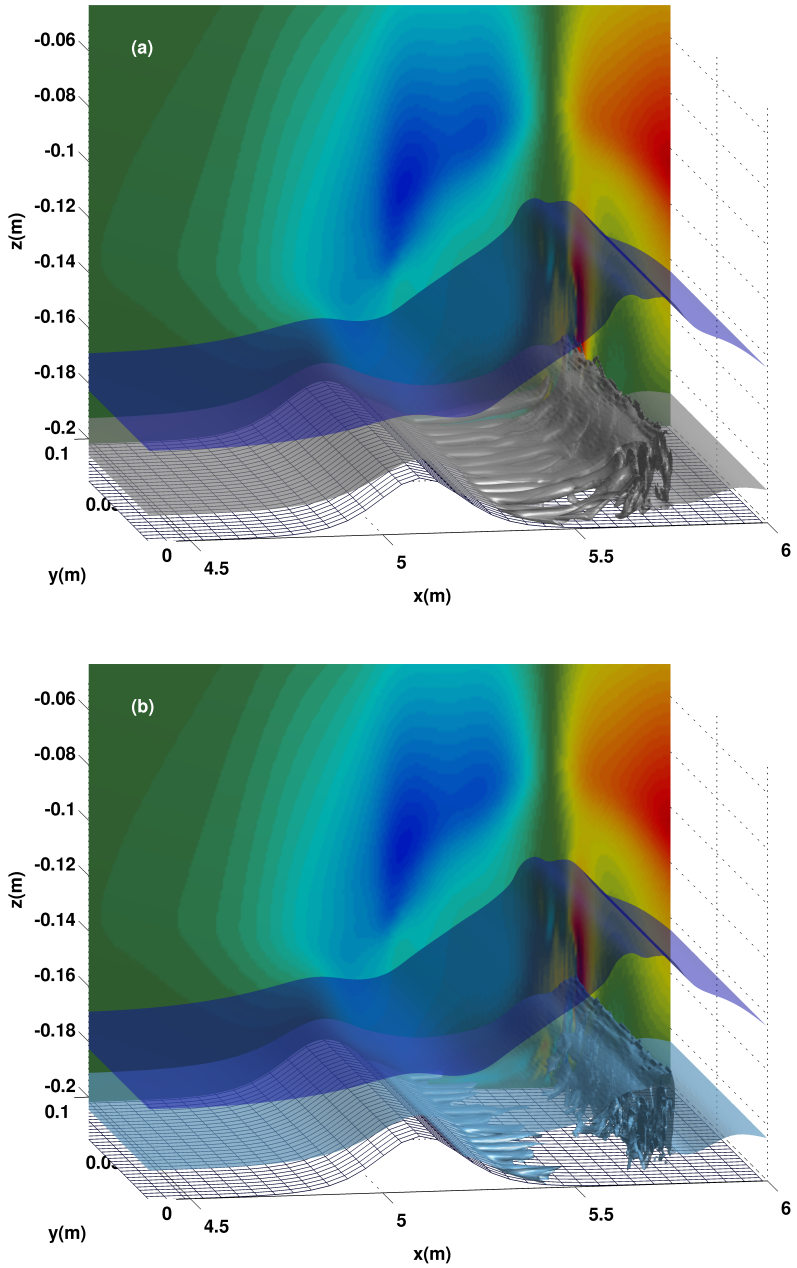

Figure 3.33: Density isosurface plots for the large perturbation run at time $t = 20$ s. The top indigo isosurface corresponds to a density value of 1.015 kg/L and the background is an $x - z$ slice of the vertical velocity. The location of the wave can be seen by the wave-induced currents (the large blue and yellow-orange regions in the background). (a) The grey isosurface corresponds to a density value of 1.022 kg/L, (b) The light blue isosurface corresponds to a density value of 1.021 kg/L.

3.5 Extensions (Scale-up)

Performing numerical simulations in an experimental set-up is without doubt, useful and necessary to provide the main picture of what can actually occur in the natural environment, while also saving on computational cost and time when compared to field-scale simulations. However, recall that this research is based upon real-world phenomena and the intention and goal is to shed light on some possible mechanisms whereby ISWs can induce sediment and cross-BBL transport when they propagate over (gentle) topography with a near-bottom stratification. For this purpose, scale-up numerical simulations were done for both an ISW of depression and elevation. The physical domain parameters for the scale-up simulations were chosen to mimic that of a shallow water lake. The reader is asked to keep in mind that performing a scale-up simulation with reasonable resolution in 2D can be quite costly computation-wise, more so for a field-scale 3D simulation. Due to the time limitations of the Master's program, only two scale-up simulations were performed and will be presented below.

3.5.1 Model Set-up and Results

The domain parameters for the shallow lake were chosen to be $H = 10$ m and $L = 125$ m, with a grid size of $N_x = 8192$ and $N_z = 512$. All of the grid types, boundary conditions and physical parameters are the same as those employed in the laboratory-scale simulations. Thus, the horizontal resolution is 1.53×10^{-2} m and the vertical resolution varies from 3.13×10^{-3} m in the near-boundary region to 3.13×10^{-2} m in the centre of the water column. There are approximately 51 points in the 0.25 m thick nepheloid layer. The single topographic hill centred at $x = 110$ m has an amplitude of 0.5 m (5% of the total water depth) and has a base of roughly 30 m. The shape of the bottom topography is specified by the expression given in (3.5.1). The larger part of the hill has a slope of about 3.5°, which is comparable to the hill used in the lab-scale simulations, with the slope near the base being less than 1°.

$$h(x) = 0.5 \operatorname{sech}^2\left(\frac{x - 110}{5}\right) \tag{3.5.1}$$

$$\bar{\rho}(z) = 1 - 0.0025 \tanh\left(z - z_0\right) - 0.00125 \tanh\left(\frac{z + 9.75}{0.1}\right) \tag{3.5.2}$$

The density profile used is given in (3.5.2), where the wave pycnocline has a 0.5% density change across a distance of 2 m. The parameter z_0 indicating the centre of this pycnocline takes on the values of -2.5 m and -7.5 m for the waves of depression and elevation, respectively. Both waves have an amplitude of 0.15 m, or 15% of the total fluid depth. The near-bottom pycnocline representing the nepheloid layer is centred at $z = -9.75$ m and has a density change of 0.25% across a 0.2 m height so that the nepheloid layer lies below the hill crest. The estimated Reynolds number based on the maximum wave-induced current below the wave pycnocline and above the nepheloid layer is $Re_w \approx 9.1 \times 10^5$, which is 65 times the corresponding Reynolds number for the lab-scale simulations, while the Reynolds number based on the jet is $Re_{jet} \approx 600$, double that in the lab-scale simulations.

The dynamics and instabilities that develop in both the depression and elevation simulations differ in some distinct ways when compared to their lab-scale counterparts. In the depression case, there are small-scale instabilities (vortex production) on the top-left side of the hill, near the crest. Figure 3.34 shows a zoomed in view of the horizontal and vertical velocities at a late time, when the instabilities have fully developed. A short summary of the events that take place as the wave moves over the hill is as follows.

The prograde jet is much thinner than the nepheloid layer: 0.03 m as opposed to 0.25 m. As the wave begins to move over the hill, the jet progresses up the left slope while the dense fluid on the right side of the hill also moves up to the hill crest, as in the lab-scale simulation. The nepheloid layer on the left, near the base of the hill, accelerates as the wave continues to propagate over the hill, resulting in what looks like a thick jet in panel (a). Only the very front edge of the dense, incoming fluid from the right just makes it over the hill crest before the wave currents decrease and cause the dense fluid to decelerate and move down the hill (the orange bulge on the right in panel (a)). The small instabilities that develop occur because of a shear instability at the interface of the original jet and leftward wave currents. This interface coincides with the interface between the light fluid above the hill boundary and the dense fluid that has moved over from the left. There is no jet roll-up at the hill crest as in the lab-scale simulation. The resulting instability produces many small vortices as shown in panels (b) and (c), that stretch from about $x = 105.7$ m to $x = 107.8$ m for the time shown. The vortex structures have a typical height of about $0.08 - 0.09$ m, with typical vertical velocities of 0.02 ms^{-1}. We can thus deduce that there will be cross-BBL transport in this field-scale set-up.

In the case of the wave of elevation, the early stages of gravity current formation, as seen in panel (a) of Figure 3.35 are also present, with the front region curling upward. However, the dense fluid at the bottom of the leading edge rolls up, entrapping light fluid and resulting in subsequent vortex production as shown in panels (b) - (d). Thus, for the times shown, it appears that the R-T instability is significantly modified by shear. This

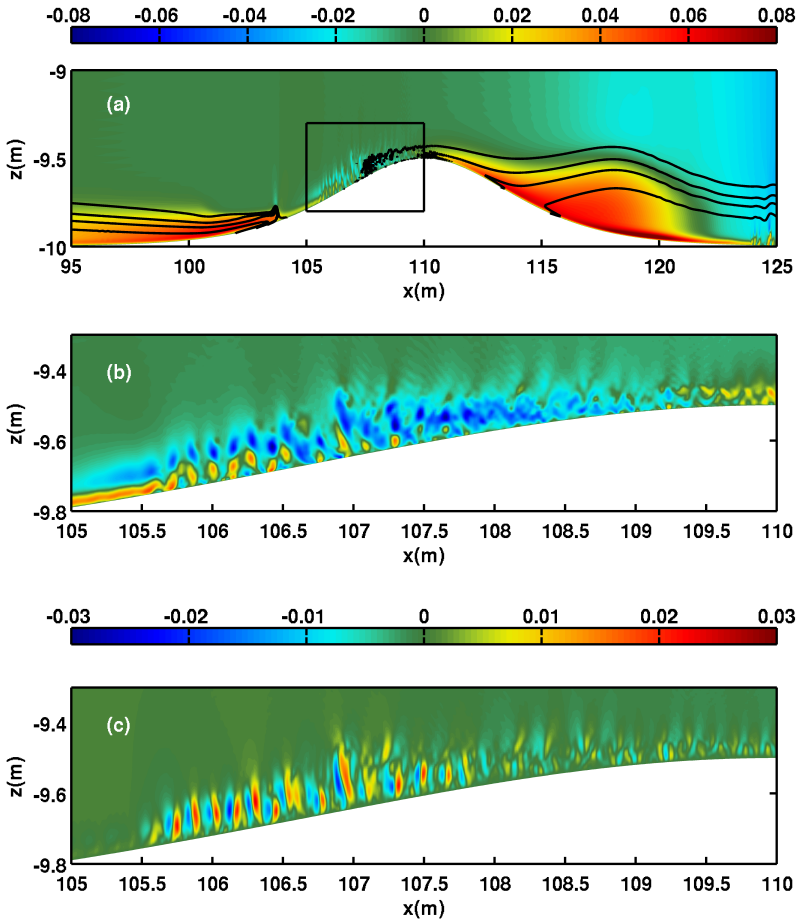

Figure 3.34: Scale-up depression case at time $t = 300$ s. Panel (a) plots the horizontal velocity saturated at 0.08 ms^{-1} for the near hill region. Density contours are overlaid in black to indicate the nepheloid layer. The black box encloses the small-scale instability on which panels (b) and (c) zooms in. Panel (b) shows the horizontal velocity saturated at 0.03 ms^{-1}; (c) is the vertical velocity saturated at 0.03 ms^{-1}.

modified R-T instability provides a means for mixing of some of the overlying light fluid with the nepheloid layer. It is possible that these vortices can induce sediment resuspension, but this is left as a future research direction. Furthermore, there is an accelerated shear layer at the top of the gravity current that appears to lead small-scale shear instability

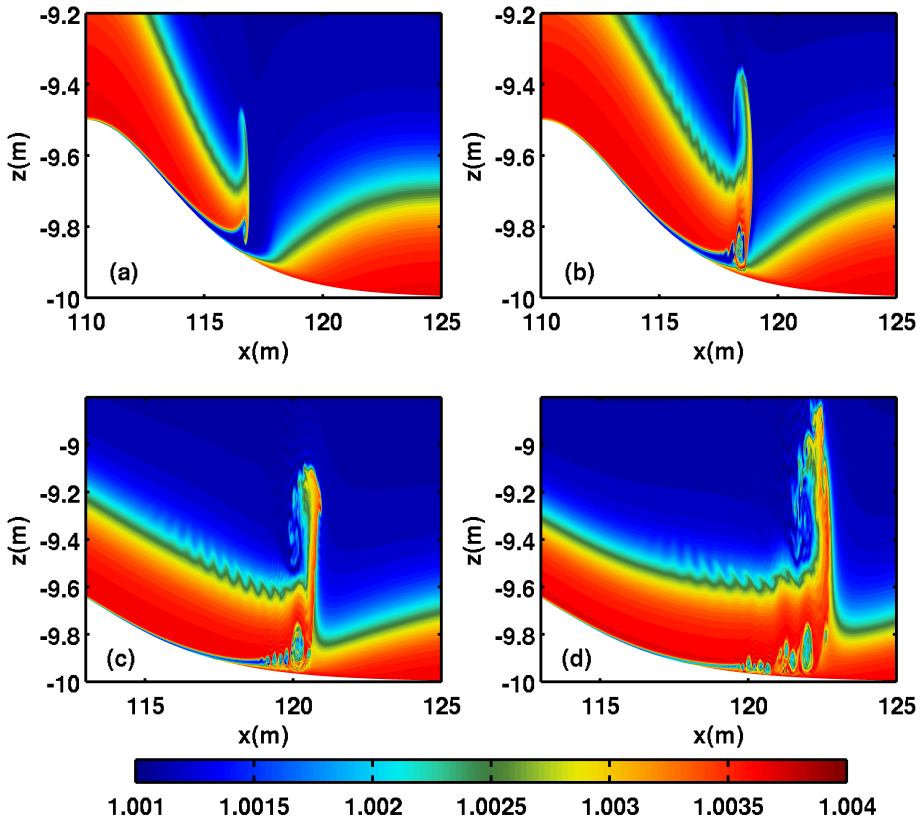

Figure 3.35: Density plots for the evolution of the instability for the the scale-up elevation simulation. (a) $t = 200$ s, (b) $t = 210$ s, (c) $t = 220$ s, (d) $t = 230$ s. Note that the subsection of the domain shown in panels (c) and (d) is slightly different to that shown in (a) and (b).

(particularly evident in the green colours in panels (c) and (d)), another contrast to the lab-scale simulations. The front portion of the current extends quite a large distance into the water column, about 1.2 m from the bottom, as illustrated in panel (d). Consequently, any suspended sediment in the nepheloid layer in this part of the gravity current can be moved higher into the water column.

Field-scale fluid flows are characterized by a much higher Reynolds number than lab-

scale flows, and the two field-scale simulations have illustrated how the dynamics can change with a larger Reynolds number. A larger Reynolds number tends to increase the amount of turbulence generated, and decreases the thickness of boundary layers and the prograde jet. It is also very probable that the size of the hill is an important factor in the observed difference in dynamics. Nevertheless, the above simulations suggest that many of the mechanisms evident in the lab-scale simulations have counterparts at the field-scale.

Chapter 4

Conclusions, Extensions, and Future Work

A discussion and summary of the findings of this research are given in the Conclusions section of this last chapter in the thesis, followed by suggestions for future directions of this work.

4.1 Conclusions

In this thesis, laboratory-scale numerical simulations of ISWs of depression and elevation propagating over a single, broad hill with a near-bottom stratification were presented. The near-bottom stratification is used to represent a BNL. Field measurements of the suspended particle concentration suggest that many BNLs may be more weakly stratified than the near-bottom stratification employed in this work. To the best of the author's knowledge, there have been no measurements of the density stratification across the edge of the BNL, only density measurements at a point. Hence the applicability of this current work to field-scale oceanography will depend on the details of the density stratification. There can exist other reasons for the formation of a near-bottom stratified region, apart from suspended particulate matter. One such reason could be the upwelling of cold ocean water onto the continental shelf in coastal regions. However, the details of this particular case were not explored, and the thesis instead focused on the laboratory relevant situation of a pre-existing near-bottom stratification.

The present work is an extension of Harnanan *et al.* (2015) [24], in which a novel instability, the jet roll-up, occurs when a sufficiently energetic wave of depression propagates

over gentle topography. In this present work, both 2D and 3D simulations were performed for each type of wave, with the inclusion of dye simulations. The dye acts as a passive tracer for the near-bottom stratification and allows us to see what happens in an unstratified near-bottom scenario. The simulations are performed on a mapped, rectangular domain with a Chebyshev grid in the vertical to enable well-resolved near-boundary dynamics. The topography used is very gentle, with a slope averaging 3.5° and an amplitude of 10% of the total water column. The near-bottom stratification lies below the hill crest with a density change of 0.8% across the pycnocline, whereas the wave pycnocline has a density change of 4%. For this particular model set-up, the passage of the ISWs of depression and elevation over the hill generates two distinct types of instabilities in the near-bottom region.

In the depression case, the prograde jet rolls up at the hill crest as in Harnanan *et al.* [24]. Because of the leftward horizontal wave currents, the dense nepheloid layer fluid on the right side of the hill is moved up to the hill crest as the jet begins to roll up. The extra energy required to lift this dense fluid results in smaller, less energetic vortices which only extend about 15% of the total depth into the water column, as opposed to an unstratified bottom represented by the dye simulation. This energy hypothesis is confirmed through time-averaged kinetic energy plots in the 2D simulations. In an unstratified bottom, the vortex structures contain typical vertical velocities of approximately double those in the bottom-stratified case, and they can extend up to 30% of the total depth into the water column from the domain bottom. This result is obtained in both the 2D and 3D simulations.

The stronger vertical velocities and greater extension into the water column suggests that an unstratified bottom will be much more efficient at cross-BBL transport when compared to having a BNL. The greater energetics increases the likelihood of sediment resuspension, but an analysis of bottom shear stress (and possibly bottom pressure) will be needed to confirm or refute this. However, with a BNL there is already suspended material, and the vortices are large enough in both the small and large perturbation cases to have the potential of pumping the previously suspended sediment about 0.02 m above the near-bottom pycnocline, which is located at $z = -0.19$ m. These instabilities are also a source of cross-BBL transport for dissolved chemical species (e.g. dissolved oxygen), and the 3D results indicate that this transport is likely to occur in a larger geographical area than in an unstratified bottom, albeit with less efficient cross-BBL transport.

The spanwise kinetic energy scaled by the maximum kinetic energy is used to assess the degree of three-dimensionalization. Application of this tool with the heuristic values used in Harnanan *et al.*, indicates that both the small and large perturbation simulations attain moderate three-dimensionalization, whereas the dye simulation remained essentially 2D even at later times in the simulation. This is in contrast to Harnanan *et al.* where moderate three-dimensionalization was attained for an unstratified near-bottom region.

The difference can be attributed to the use of a larger and more energetic wave (and hence a larger and more energetic prograde jet) in Harnanan *et al.* The small noise simulation takes a longer time to attain moderate three-dimensionalization when compared to the large noise simulation, and the area containing three-dimensionalization is smaller. Nevertheless, the vertical velocities in the near-bottom region are comparable in magnitude to those in the large noise simulation.

With the ISW of elevation, unlike with the wave of depression, the instability that arises is solely a consequence of having a near-bottom stratification. As the wave passes over the hill, the crest of dense nepheloid layer fluid shoals, and the horizontal difference in the fluid densities across the topographic crest leads to the formation of a gravity current. This is a novel type of gravity current because there is the influence of the wave-induced currents. It is also short-lived, and the instability that results in what was once the front region of the current is essentially a variant of the Rayleigh-Taylor instability. The 2D simulations reveal that this instability region moves along with the wave for some distance (at least 2 m from the hill crest) before it is dissipated. This mechanism thus provides a means for the transportation of nepheloid layer fluid that has been mixed with the overlying fluid. The gravity current formation and subsequent R-T instability is absent in both the 2D and 3D dye simulations, although some vortex production does occur on the right slope of the hill in the 2D case, long after the wave has cleared the hill.

Both the 3D small and large perturbation simulations show that the R-T instability and mixing begins at an earlier time than in their 2D counterpart. The mixing that occurs in the 3D simulations is intense, especially in the large perturbation case where it is highly turbulent. The majority of this mixing occurs in the front region of the gravity current, a result that is consistent with previous studies [59, 26, 25]. There is an absence of Kelvin-Helmholtz instabilities and billow formation, but the lobe-cleft instability is present for both the small and large noise simulations. Three-dimensionalization sets in approximately 2.5 s later for the small noise simulation versus the large noise simulation. Although the degree of three-dimensionalization is significant in both cases, the instability region is larger in both the $x-$ and $z-$directions and is more energetic for the large noise case, indicating more cross-BBL transport and mixing in a larger geographical region. Note that the vertical velocities in the instability region near the bottom are comparable and very close for the two cases, so that over a given area they can both induce similar amounts of cross-BBL transport.

As we can see from both the waves of depression and elevation, reducing the perturbation by two orders of magnitude delays the onset of three-dimensionalization and reduces the geographical area of the instability region. However, the results for the particular model set-up in this work suggest that the qualitative behaviour of the instability is maintained

in the small noise case. The velocities in the instability region near the bottom boundary, particularly the vertical velocities, are comparable for the two noise simulations. Perturbations in the natural world have a variety of sources, but the qualitative consistency of the results suggests that they should be readily observable.

4.2 Future Work

As with almost any aspect of research, the work in this thesis is by no means complete, and therefore leads to various future research directions. As mentioned, calculations of the bed shear stress in both the laboratory and field-scale simulations will allow a conclusion to be drawn on the likelihood of sediment resuspension. Further field-scale simulations at higher resolutions are probably warranted as some of the instabilities formed are quite small-scale. Performing laboratory-scale numerical simulations at a higher Reynolds number would be very worthwhile, since field-scale flows have higher Reynolds numbers than those in the current laboratory-scale simulations.

The parameter space for large-scale flows such as in this thesis, is large. There are therefore are many different parameter choices that one can consider. For instance, varying the height of the near-bottom pycnocline with a fixed hill and wave would be a practical and worthwhile pursuit, as the BNL thickness can change throughout the same day. The broad range of definitions of a BNL also suggests that varying the strength of the near-bottom pycnocline would prove to be a useful research direction. The reader should note that the strength of the near-bottom stratification used in this work is stronger than some of the measured sediment concentrations in the field [27, 28, 69, 53], so that simulations with weaker stratifications will need to be explored, particularly for the elevation case as the instability depends on the near-bottom density differences. A small suite of simulations of the wave of depression (not presented in the thesis) has shown the vortices to become larger and move higher into the water column as the bottom stratification becomes weaker, thereby increasing the efficiency of cross-BBL transport.

Performing laboratory experiments would be very useful for comparison purposes. It may also be interesting to perform a simulation with just a horizontal forcing representative of a tide, in order to determine how much of the dynamics are due to the ISW.

References

[1] Snezhana I Abarzhi, Serge Gauthier, and Robert Rosner. Turbulent mixing and beyond. *Physica Scripta*, 2008(T132):011001, 2008.

[2] Payam Aghsaee and Leon Boegman. Experimental investigation of sediment resuspension beneath internal solitary waves of depression. *Journal of Geophysical Research: Oceans*, 120(5):3301–3314, 2015.

[3] Payam Aghsaee, Leon Boegman, Peter J Diamessis, and Kevin G Lamb. Boundary-layer-separation-driven vortex shedding beneath internal solitary waves of depression. *Journal of Fluid Mechanics*, 690:321–344, 2012.

[4] Silvia Albarracín, Javier Alcántara-ió, Isabel Montoya-Montes, Ángela Fontán-Bouzas, Luis Somoza, Carl L Amos, and Jorge Rey Salgado. Relict sand waves in the continental shelf of the Gulf of Valencia (Western Mediterranean). *Journal of Sea Research*, 2014.

[5] Malcolm J Andrews and Stuart B Dalziel. Small Atwood number Rayleigh–Taylor experiments. *Philosophical Transactions of the Royal Society of London A: Mathematical, Physical and Engineering Sciences*, 368(1916):1663–1679, 2010.

[6] Nicole J Baeten, Jan Sverre Laberg, Matthias Forwick, Tore O Vorren, Maarten Vanneste, Carl Fredrik Forsberg, Tore J Kvalstad, and Michael Ivanov. Morphology and origin of smaller-scale mass movements on the continental slope off northern Norway. *Geomorphology*, 187:122–134, 2013.

[7] Peter G Baines. Mixing in downslope flows in the ocean-plumes versus gravity currents. *Atmosphere–Ocean*, 46(4):405–419, 2008.

[8] Joel E Baker, Steven J Eisenreich, and Brian J Eadie. Sediment trap fluxes and benthic recycling of organic carbon, polycyclic aromatic hydrocarbons, and polychlorobiphenyl congeners in lake superior. *Environmental Science & Technology*, 25(3):500–509, 1991.

[9] D Bourgault, MD Blokhina, R Mirshak, and DE Kelley. Evolution of a shoaling internal solitary wavetrain. *Geophysical Research Letters*, 34(3), 2007.

[10] Daniel Bourgault, M Morsilli, Clark Richards, U Neumeier, and Dan E Kelley. Sediment resuspension and nepheloid layers induced by long internal solitary waves shoaling orthogonally on uniform slopes. *Continental Shelf Research*, 72:21–33, 2014.

[11] S Burgmann, Ch Brücker, and W Schröder. Scanning PIV measurements of a laminar separation bubble. *Experiments in Fluids*, 41(2):319–326, 2006.

[12] W Cabot. Comparison of two-and three-dimensional simulations of miscible Rayleigh-Taylor instability. *Physics of Fluids (1994-present)*, 18(4):045101, 2006.

[13] William H Cabot and Andrew W Cook. Reynolds number effects on Rayleigh–Taylor instability with possible implications for type ia supernovae. *Nature Physics*, 2(8):562–568, 2006.

[14] David Cacchione and Lincoln Pratson. Internal Tides and the Continental Slope Curious waves coursing beneath the surface of the sea may shape the margins of the world's landmasses. *American scientist*, 92(2):130–137, 2004.

[15] Magda Carr, Peter A Davies, and Pruthvi Shivaram. Experimental evidence of internal solitary wave-induced global instability in shallow water benthic boundary layers. *Physics of Fluids (1994-present)*, 20(6):066603, 2008.

[16] SB Dalziel, PF Linden, and DL Youngs. Self-similarity and internal structure of turbulence induced by Rayleigh–Taylor instability. *Journal of Fluid Mechanics*, 399:1–48, 1999.

[17] Peter J Diamessis and Larry G Redekopp. Numerical investigation of solitary internal wave-induced global instability in shallow water benthic boundary layers. *Journal of Physical Oceanography*, 36(5):784–812, 2006.

[18] Timothy F Duda, James F Lynch, James D Irish, Robert C Beardsley, Steven R Ramp, Ching-Sang Chiu, Tswen Yung Tang, and Ying-Jang Yang. Internal tide and nonlinear internal wave behavior at the continental slope in the northern South China Sea. *Oceanic Engineering, IEEE Journal of*, 29(4):1105–1130, 2004.

[19] Micheal Dunphy, Christopher Subich, and Marek Stastna. Spectral methods for internal waves: indistinguishable density profiles and double-humped solitary waves. *Nonlinear Processes in Geophysics*, 18(3):351–358, 2011.

[20] Roger D Flood, Alexander N Shor, and Patricia L Manley. Morphology of abyssal mudwaves at Project MUDWAVES sites in the Argentine Basin. *Deep Sea Research Part II: Topical Studies in Oceanography*, 40(4):859–888, 1993.

[21] Marcelo H García. Sedimentation and erosion hydraulics. *Hydraulic design handbook*, pages 1–112, 1999.

[22] Michael Gaster. *The structure and behaviour of laminar separation bubbles*. Citeseer, 1969.

[23] Neil D Graham, Serge Stoll, and Jean-Luc Loizeau. Colloid characterization at the sediment-water interface of Vidy Bay, Lake Geneva. *Fundamental and Applied Limnology/Archiv für Hydrobiologie*, 184(2):87–100, 2014.

[24] Sandhya Harnanan, Nancy Soontiens, and Marek Stastna. Internal wave boundary layer interaction: A novel instability over broad topography. *Physics of Fluids (1994-present)*, 27(1):016605, 2015.

[25] Carlos Hartel, Fredrik Carlsson, and Mattias Thunblom. Analysis and direct numerical simulation of the flow at a gravity-current head. Part 2. The lobe-and-cleft instability. *Journal of Fluid Mechanics*, 418(213-229):29, 2000.

[26] Carlos Härtel, Eckart Meiburg, and Frieder Necker. Analysis and direct numerical simulation of the flow at a gravity-current head. Part 1. Flow topology and front speed for slip and no-slip boundaries. *Journal of Fluid Mechanics*, 418:189–212, 2000.

[27] Nathan Hawley and CR Murthy. The response of the benthic nepheloid layer to a downwelling event. *Journal of Great Lakes Research*, 21(4):641–651, 1995.

[28] Nathan Hawley and Ronald W Muzzi. Observations of nepheloid layers made with an autonomous vertical profiler. *Journal of Great Lakes Research*, 29(1):124–133, 2003.

[29] Karl R Helfrich and W Kendall Melville. Long nonlinear internal waves. *Annu. Rev. Fluid Mech.*, 38:395–425, 2006.

[30] Karl R Helfrich and WK Melville. On long nonlinear internal waves over slope-shelf topography. *Journal of Fluid Mechanics*, 167:285–308, 1986.

[31] Patrick Jones, Kanchan Maiti, and J McManus. Lead-210 and polonium-210 disequilibria in the northern Gulf of Mexico hypoxic zone. *Marine Chemistry*, 169:1–15, 2015.

[32] Jody M Klymak and James N Moum. Internal solitary waves of elevation advancing on a shoaling shelf. *Geophysical Research Letters*, 30(20), 2003.

[33] Pijush K. Kundu, Ira M. Cohen, and David R. Dowling. *Fluid Mechanics*. Academic Press, fifth edition, 2012.

[34] Kevin G Lamb. On the calculation of the available potential energy of an isolated perturbation in a density-stratified fluid. *Journal of Fluid Mechanics*, 597:415–427, 2008.

[35] Kevin G Lamb. Internal wave breaking and dissipation mechanisms on the continental slope/shelf. *Annual Review of Fluid Mechanics*, 46:231–254, 2014.

[36] Kevin G Lamb and Bangjun Wan. Conjugate flows and flat solitary waves for a continuously stratified fluid. *Physics of Fluids (1994-present)*, 10(8):2061–2079, 1998.

[37] Kevin G Lamb and Liren Yan. The evolution of internal wave undular bores: comparisons of a fully nonlinear numerical model with weakly nonlinear theory. *Journal of Physical Oceanography*, 26(12):2712–2734, 1996.

[38] KG Lamb. Extreme internal solitary waves in the ocean: Theoretical considerations. *Preprint University of Waterloo*, pages 109–117, 2006.

[39] Andrew GW Lawrie and Stuart B Dalziel. Turbulent diffusion in tall tubes. I. Models for Rayleigh-Taylor instability. *Physics of Fluids (1994-present)*, 23(8):085109, 2011.

[40] Jason Link. Benthic nepheloid layers in central and western Lake Superior. *Journal of Great Lakes Research*, 20(4):667–670, 1994.

[41] Anthony K Liu, Y Steve Chang, Ming-K Hsu, and Nai K Liang. Evolution of nonlinear internal waves in the East and South China Seas. *Journal of Geophysical Research*, 103:7995–8008, 1998.

[42] Vladimir Maderich, Tatiana Talipova, Roger Grimshaw, Katherina Terletska, Igor Brovchenko, Efim Pelinovsky, and Byung Ho Choi. Interaction of a large amplitude interfacial solitary wave of depression with a bottom step. *Physics of Fluids (1994-present)*, 22(7):076602, 2010.

[43] IN McCave. Local and global aspects of the bottom nepheloid layers in the world ocean. *Netherlands Journal of Sea Research*, 20(2):167–181, 1986.

[44] Alena Mudroch and Paul Mudroch. Geochemical composition of the nepheloid layer in Lake Ontario. *Journal of Great Lakes Research*, 18(1):132–153, 1992.

[45] RJ Munro, N Bethke, and SB Dalziel. Sediment resuspension and erosion by vortex rings. *Physics of Fluids*, 21(4):046601, 2009.

[46] Robert J Munro. The interaction of a vortex ring with a sloped sediment layer: Critical criteria for incipient grain motion. *Physics of Fluids*, 24(2):026604, 2012.

[47] Jason Olsthoorn and Marek Stastna. Numerical investigation of internal wave-induced sediment motion: Resuspension versus entrainment. *Geophysical Research Letters*, 41(8):2876–2882, 2014.

[48] Laura L Pauley, Parviz Moin, and William C Reynolds. The structure of two-dimensional separation. *Journal of Fluid Mechanics*, 220:397–411, 1990.

[49] CH Pilskaln, K Hayashi, BA Keafer, DM Anderson, and DJ McGillicuddy. Benthic nepheloid layers in the Gulf of Maine and Alexandrium cyst inventories. *Deep Sea Research Part II: Topical Studies in Oceanography*, 103:55–65, 2014.

[50] R Porter-Smith, VD Lyne, RJ Kloser, and VL Lucieer. Catchment-based classification of Australia's continental slope canyons. *Marine Geology*, 303:183–192, 2012.

[51] Martina Preusse, Heinrich Freistühler, and Frank Peeters. Seasonal variation of solitary wave properties in Lake Constance. *Journal of Geophysical Research: Oceans*, 117(C4), 2012.

[52] Pere Puig, Xavier Durrieu de Madron, Katrin Schroeder, Jordi Salat, José Luis López-Jurado, Gian P Gasparini, Albert Palanques, and Mikhail Emelianov. Formation of a basin-wide bottom nepheloid layer in the western Mediterranean after winter 2005 dense shelf water cascading event. *Geo-Temas*, 11:141–142, 2010.

[53] Luis Santos Quaresma, João Vitorino, Anabela Oliveira, and José da Silva. Evidence of sediment resuspension by nonlinear internal waves on the western Portuguese mid-shelf. *Marine Geology*, 246(2):123–143, 2007.

[54] Marta Ribó, Pere Puig, J Salat, and A Palanques. Nepheloid layer distribution in the Gulf of Valencia, northwestern Mediterranean. *Journal of Marine Systems*, 111:130–138, 2013.

[55] Carlo Scalo, Ugo Piomelli, and Leon Boegman. High-schmidt-number mass transport mechanisms from a turbulent flow to absorbing sediments. *Physics of Fluids (1994-present)*, 24(8):085103, 2012.

[56] Alberto Scotti and Jesús Pineda. Observation of very large and steep internal waves of elevation near the Massachusetts coast. *Geophysical Research Letters*, 31(22), 2004.

[57] David H Sharp. An overview of Rayleigh-Taylor instability. *Physica D: Nonlinear Phenomena*, 12(1):3–18, 1984.

[58] JO Shin, SB Dalziel, and PF Linden. Gravity currents produced by lock exchange. *Journal of Fluid Mechanics*, 521:1–34, 2004.

[59] John E Simpson. *Gravity currents: In the environment and the laboratory*. Cambridge University Press, second edition, 1997.

[60] Nancy Soontiens, Marek Stastna, and Michael L Waite. Topographically generated internal waves and boundary layer instabilities. *Physics of Fluids (1994-present)*, 27(8):086602, 2015.

[61] Marek Stastna and Kevin G Lamb. Large fully nonlinear internal solitary waves: The effect of background current. *Physics of Fluids (1994-present)*, 14(9):2987–2999, 2002.

[62] Marek Stastna and Kevin G Lamb. Sediment resuspension mechanisms associated with internal waves in coastal waters. *Journal of Geophysical Research: Oceans (1978–2012)*, 113(C10), 2008.

[63] Christopher Subich. Simulation of the Navier-Stokes equations in three dimensions with a spectral collocation method. 2011.

[64] C.J. Subich, K.G. Lamb, and M. Stastna. Simulation of the Navier-Stokes equations in three dimensions with a spectral collocation method. *Int. J. Numer. Meth. Fluids*, 73:103–129, 2013.

[65] Tatiana Talipova, Katherina Terletska, Vladimir Maderich, Igor Brovchenko, Kyung Tae Jung, Efim Pelinovsky, and Roger Grimshaw. Internal solitary wave transformation over a bottom step: Loss of energy. *Physics of Fluids (1994-present)*, 25(3):032110, 2013.

[66] Mark V Trevorrow. Observations of internal solitary waves near the Oregon coast with an inverted echo sounder. *Journal of Geophysical Research: Oceans*, 103(C4):7671–7680, 1998.

[67] Maurice E Tucker. *Sedimentary petrology: an introduction to the origin of sedimentary rocks*. John Wiley & Sons, 2009.

[68] B Turkington, A Eydeland, and S Wang. A computational method for solitary internal waves in a continuously stratified fluid. *Studies in Applied Mathematics*, 85(2):93–127, 1991.

[69] Noel R Urban, J Jeong, and Yingtao Chai. The benthic nepheloid layer (BNL) north of the Keweenaw Peninsula in Lake Superior: composition, dynamics, and role in sediment transport. *Journal of Great Lakes Research*, 30:133–146, 2004.

[70] David L Youngs. Numerical simulation of turbulent mixing by Rayleigh-Taylor instability. *Physica D: Nonlinear Phenomena*, 12(1):32–44, 1984.